ORNL/TM-2022/2474
Final CRADA - NFE-19-07528

Predictive Tools for Customizing Heat Treatment of Additively Manufactured Aerospace Components

Balasubramaniam Radhakrishnan
Younggil Song
Sarma Gorti
Ranadip Acharya

May 2022

OAK RIDGE National Laboratory

ORNL IS MANAGED BY UT-BATTELLE LLC FOR THE US DEPARTMENT OF ENERGY

ORNL/TM-2022/2474
FINAL CRADA – NFE-19-07528

High Performance Computing for Energy Innovation (HPC4EI) Report

PREDICTIVE TOOLS FOR CUSTOMIZING HEAT TREATMENT OF ADDITIVELY MANUFACTURED AEROSPACE COMPONENTS

Balasubramaniam Radhakrishnan and Sarma Gorti
Computational Sciences and Engineering Division, Oak Ridge National Laboratory
Younggil Song, Lawrence Livermore National Laboratory
Ranadip Acharya, Collins Aerospace Applied Research and Technology

May 2022

Prepared by
OAK RIDGE NATIONAL LABORATORY
Oak Ridge, TN 37831
managed by
UT-BATTELLE LLC
for the
US DEPARTMENT OF ENERGY
under contract DE-AC05-00OR22725

CONTENTS

LIST OF FIGURES

LIST OF TABLES

ABSTRACT

Laser-bed powder fusion (LBPF) additive manufacturing is increasingly being used to produce components of complex geometries using the Ni-base superalloy Inconel 718. The composition and the microstructure of the alloy are currently well optimized for wrought components made using conventional manufacturing processes such as rolling, forging, extrusion, etc. The attractive mechanical properties of the alloy result from the underlying austenitic matrix with fine equiaxed grains, and a high density and uniform distribution of the precipitation hardening phase, γ". Heat treatment steps such as homogenization, solutioning and aging are well documented for the wrought alloy. However, when the same wrought alloy compositions are used for the additive manufacturing (AM) processes, the as-processed microstructure is significantly different, because of the different thermal history associated with LBPF, including rapid solidification and multiple temperature excursions that lead to multiple re-melting and reheating in the solid state. Rapid solidification introduces potential non-equilibrium effects at the moving solid-liquid interfaces that impact the extent of solute segregation, as well as the morphology of the dendritic grains that form. In order to recover the target mechanical properties, AM components have to undergo post-process heat treatments. However, such heat treatments have to be custom designed for the AM process and the component geometry because of the expected vast differences in the microstructure at various locations of a component with complex geometry. The homogenization and precipitation steps should be optimized for the component so that target mechanical properties can be obtained throughout the part. The objective of this research is to utilize High Performance Computing in phase field simulations of microstructure evolution during post-processing of AM components. The physics-based modeling will be beneficial in reducing the experimental effort required for heat treatment process selection, optimization, and certification, thus leading to a significant reduction in energy consumption for AM and post-processing heat treatment. The optimization study will help identify heat treatments steps that are critical for development of a final desired microstructure with the minimum energy input. This combined with shortening of the production cycle (time-to-market) by reducing the number of failed parts (property targets), and reduction in the number of iterations for process optimization, will enable 30-40% savings in the energy costs. Phase field simulations of the degree of homogenization and the effect of local matrix composition on the nucleation and growth of competing precipitating phases were performed using the Microstructure Evolution Using Massively Parallel Phase Field Simulations code developed in-house at the Oak Ridge National Laboratory. The simulations were able to successfully capture the kinetics of nucleation and growth, and morphologies of various precipitating phases as a function of local matrix compositions and composition gradients characteristic of local microstructures arising from location-dependent variations in the thermal conditions. Future work will involve extending the simulations to a length scale consisting of multiple dendrites, so that the effect of homogenization on the coarsening of the dendrites can be simulated and used as an additional input to the optimization of the heat treatment process.

1. INTRODUCTION

The computational objective of this project is to perform high performance computing (HPC) based phase-field simulations of solid-state precipitation in additive manufacturing (AM) processed IN718 alloy using the Microstructure Evolution Using Massive Parallel Phase-field Simulations – Solid State (MEUMAPPS-SS) phase field code to capture the effect of the expected variabilities in the microstructural features at various locations within an AM component on the phase selection, morphology, nucleation, and growth kinetics of competing phases. The simulations were limited to the length scale of a single dendrite because of the need to perform three-dimensional simulations with a high spatial resolution requirement that are computationally very expensive. Within the length scale of a dendrite, the main microstructural variables that were considered included the local solute concentration at an inter-dendritic location that is enriched due to the prevailing micro-segregation, and the solute concentration gradient arising from the local secondary arm spacing that is determined by the local solidification rate at a location within the component. Concentration gradients arising from the dissolution of the Laves phase that is typically found in the as-solidified microstructure was also considered. Another important microstructural feature considered in the simulations is the presence of dislocations and the effect of the strain field of the dislocations on phase selection and kinetics of precipitation. Additive manufacturing experiments, heat treatments, and the characterization of the resulting microstructures were performed at United Technologies Research Center (UTRC) in order to provide inputs for the phase field simulations as well as to validate some of the phase field simulation results.

The computational motivation for the proposed modeling effort is to demonstrate the capabilities of the phase field simulation technique and the use of leadership class, high-performance computing capabilities in capturing the mesoscale physics associated with solid-state transformations to quantify microstructural evolution during post-process annealing of AM microstructures. From a technology standpoint, the challenge is to design an optimum post-processing heat treatment for an AM component with a complex geometry. Since the local, as-formed microstructure with a complex AM component varies according to the local thermal conditions, the challenge is the custom-design of a microstructure that is optimum for the entire component. Although this task is beyond the scope of the current project, the simulations performed as part of this project will form the basis for tackling such an objective in the future. Specifically, the simulations allow for the optimization of the mechanical properties of AM materials by exploiting the emerging science of gradient materials. The length scale of the gradients could be varied by partial homogenization of the as-formed microstructure and precipitation inside the solute gradient could be achieved by direct aging. Such an approach will lead to significant energy savings associated with full homogenization and also help to preserve the ultra-fine microstructure that is produced during AM due to rapid solidification.

2. RESULTS

The results obtained during this project for the various tasks as presented in the Statement of Work (SOW) are presented in this section.

2.1 TASK 1. EXPERIMENTAL INPUT FOR PHASE FIELD MODELING AND VALIDATION

Objective: Generate experimental data that will be used as input microstructures for the model, and also generate microstructural data after heat treatment processes that will be used as input for model validation.

Progress: As part of this effort, UTRC performed the following experiments and associated characterization studies in their research facilities:

Single track IN718 Laser Powder Bed Fusion (LPBF) deposits were made with EOS M280 system and characterization of micro-segregation of alloying elements was accomplished using Energy Dispersive Spectroscopy (EDS) line scans across primary and secondary dendrite arms in the transverse cross-sections. These experiments were performed using two different power levels and welding speeds. One of the single-track specimens was imaged using a Helios Nanolab 600 dual beam microscope (FEI; Hillsboro, OR). The gallium ion beam was employed to local etch the surface of the coupon to discern dendrites better. The composition was probed using an X-MaxN 80 EDS unit (Oxford Instruments; Concord, Massachusetts). Table 1 summarizes the results obtained using these studies.

Table 1. AM process parameters and solidification microstructural features

Welding Condition	Primary arm spacing (nm)	Secondary arm spacing (nm)	Nb conc. across primary (wt.%)	Nb conc. across secondary (wt.%)
180W 600 mm/s	550-600	250-300	3.5 to 4 – core 6.5-8 - center	3.5 to 4 – core > 7.0 - center
285 W 960 mm/s	700-800	350-400	3.5 – core 8.5 - center	4.5 – core 7-8 center

Subsequently, the analysis of the solidification microstructure and the micro segregation pattern was extended to multi-layer AM builds using LPBF with two different deposition techniques – a default line strategy and a novel 'active melt pool' based scan strategy. While the default scan strategy showed finer dendrites with a secondary arm spacing of 200-400 nm with secondary arm formation, the 'active melt-pool' based scan strategy was found to produce coarse columnar dendrites with a primary arm spacing of greater than 1000 nm with no secondary arms. Figure 1 summarizes the findings of this work.

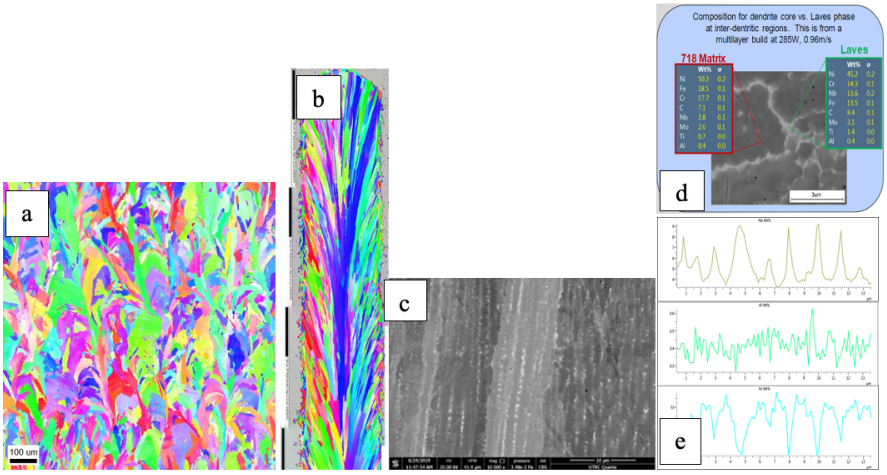

Figure 1. (a) EBSD map using default scan strategy showing finer grains, (b) EBSD map with 'active melt pool' base scan strategy, (c) columnar dendritic structure due to 'active melt pool' scan strategy, (d) segregation pattern using default scan strategy and (e) segregation pattern using 'active melt pool' based scan strategy.

An important feature of the solidification structure of IN718 is the formation of the inter-dendritic Laves phase in certain locations. Laves phase forms if the local solidification history is such that some amount of liquid exists at the terminal eutectic temperature of IN718 below which the liquid transforms to γ + Laves.

In addition to the above experiments and characterization on the as-fabricated materials, UTRC also conducted post-process heat treatments followed by microstructural characterization for various heat treatments including stress relief, hot isostatic pressing (HIP), solution annealing, and aging. The following conclusions were reached based on these experiments:

The microstructure after stress-relief was similar to the as-built microstructure with more secondary phases, particularly on the grain boundaries but also in the interdendritic regions. Interdendritic regions enriched with Nb showed precipitation of the δ phase. The microstructure after HIP showed at a larger length scale, recrystallized grains with a grain size of roughly 50-100 micrometers with δ phase precipitation on grain boundaries. The grain interior showed co-precipitation of γ', γ'', and δ phases. The microstructure after solution annealing and aging still maintained the same grain size as HIP and retained the intragranular and intergranular precipitation of δ phases although the mixture of γ', γ'' phases was much finer than in the HIP condition. Figures 2 – 4 show some of the typical microstructures obtained for the above post-processing heat treatments.

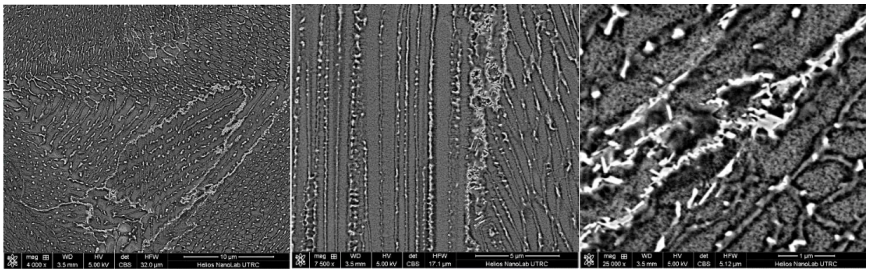

Figure 2. Microstructure after stress relief showing inter-dendritic Laves and areas with δ phase.

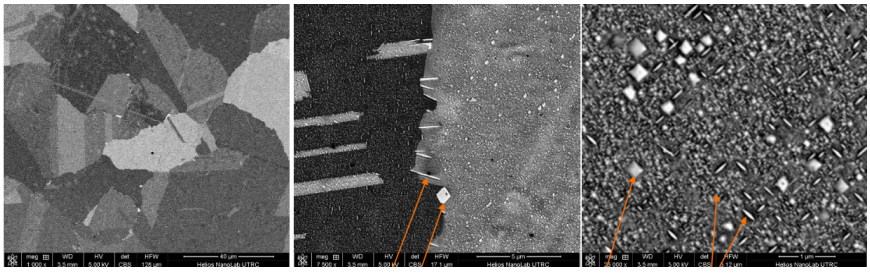

Figure 3. Microstructure after HIP showing recrystallized grains with intragranular co-precipitation of γ', γ'' and δ phases.

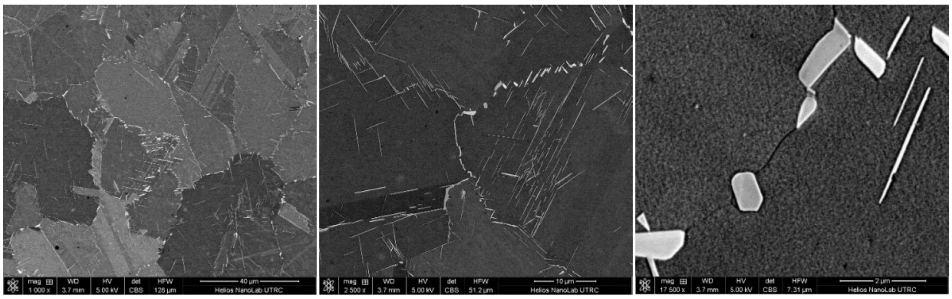

Figure 4. Microstructure after full heat treatment (solution treatment + aging) showing grain boundary and interior δ. Fine precipitation inside the grains cannot be resolved at the magnification used.

Taken together, these heat treatments indicate the possibility of multiple phase co-precipitation in the microstructures with a Nb gradient. It is also noteworthy that the δ phase that typically forms on the grain boundaries in wrought 718 forms in the intragranular regions in AM formed 718. The important inputs to the phase field simulations based on the experimental work at UTRC included the length scales of the primary and the secondary arm spacing, the need to include Laves phase in certain regions of the microstructure, and the need to handle the co-precipitation of several phases even at the length scale of a single dendrite. The main computational focus of the phase field simulations is to demonstrate these capabilities and at least qualitatively capture the co-precipitation of multiple phases.

2.2 TASK 2: DEVELOP FREE ENERGY FUNCTIONS FOR RELEVANT PRECIPITATE PHASES IN MODEL PSEUDO-TERNARY ALLOYS

Objective: The objective is to generate the Gibbs free energy functions for the competing transforming phases in the alloy using a thermodynamics database.

Progress: The MEUMAPPS phase field simulations require the Gibbs free energies of a phase at a given temperature to perform quantitative simulations. The nickel alloy database TCNI8 in the ThermoCalc software was used to estimate thermodynamic properties of surrogate ternary alloys. The nominal composition of IN718 is w(Ni)=0.525, w(Cr) = 0.19, w(Mo) = 0.0305, w(Ti) = 0.009, w(Al) = 0.002, and balance Fe, which was used to estimate the thermodynamic properties of IN718. The Nb concentration in the AM solidified microstructure was shown experimentally to vary from the core to the center of the dendrite due to micro segregation. Therefore, various Nb concentrations that are higher and lower than the nominal w(Nb) = 0.05125 in weight fraction were used in IN718 to represent various regions in the interdendritic space. The thermodynamic state of these compositions with respect to the type and equilibrium volume fraction of phases at different temperatures was calculated using ThermoCalc. Equilibrium states of Ni-base model ternary alloys Ni-Al-Nb and Ni-Fe-Nb were used as surrogate alloys for IN718. Thermodynamic calculations were performed to identify equivalent ternary alloy compositions corresponding to the IN718 alloy compositions. After establishing the feasibility of this approach, the Gibbs free energies of various phases in the model ternary systems were obtained for specified composition ranges for the two solutes and the results for each phase was fitted to a polynomial function of the two solute concentrations. The model ternary systems included Al-Nb-Ni and Fe-Nb-Ni.

2.2.1 Al-Nb-Ni

We use an Al-Nb-Ni alloy with Ni as the matrix, and Al and Nb as the two solutes. Initially the feasibility of representing the phase fractions and compositions of various phases in IN718 through model ternary was demonstrated as follows. ThermoCalc was used to calculate the type and volume fraction of phases for the nominal composition of IN718 at 740°C. This temperature was chosen because the γ' and γ" phases appeared at a temperature between 700°C and 800°C in previous studies. The Al and Nb concentrations of the Ni-Al-Nb ternary alloy that showed the same type and volume fraction of phases 740°C was searched using ThermoCalc. The exercise was repeated for IN718 compositions with different Nb concentrations. The results are listed in Tables 2 and 3 below. The compositions are listed as mole fractions. The nominal compositions of Nb and Al for IN718 are x(Nb) = 3.13214E-2 and x(Al) = 4.31391E-3. Using Tables 2 and 3, we can interpolate which concentration set of the ternary alloy corresponds to IN718. In Table 2, the first two rows show the Nb and Al concentrations in IN718. The third and fourth rows show equivalent concentrations in the ternary system such that the phase fractions of γ and δ are the same for the two alloys, shown in the last two rows. In Table 3, the delta phase was suspended, and the compositions corresponding to same volume fractions of γ, γ' and γ" phases between IN718 and the ternary alloy were calculated.

Table 2. Equivalent IN 718 and Ni-Al-Nb compositions for the constant γ and δ phase fractions

IN718	x(Nb)	2.49534E-2	3.13214E-2	3.77426E-2	6.39725E-2	9.80396E-2	1.33617E-1
	x(Al)	4.29605E-3	4.31391E-3	4.33192E-3	4.40548E-3	4.50101E-3	4.60078E-3
Ternary	x(Nb)	7.39555E-2	7.93827E-2	8.46778E-2	0.1057076	0.13263898	0.16062339
	x(Al)	3.68075E-2	3.56700E-2	3.45602E-2	3.01526E-2	2.45081E-2	1.86429E-2
Phase	γ	8.71209E-1	8.42342E-1	8.14178E-1	7.02323E-1	5.59078E-1	4.10232E-1
	δ	1.28791E-1	1.57658E-1	1.85822E-1	2.97677E-1	4.40922E-1	5.89768E-1

Table 3. Equivalent IN 718 and Ni-Al-Nb compositions for constant γ, γ' and γ" phase fractions

IN718	x(Nb)	2.49534E-2	3.13214E-2	3.77426E-2	6.39725E-2	9.80396E-2	1.33617E-1
	x(Al)	4.29605E-3	4.31391E-3	4.33192E-3	4.40548E-3	4.50101E-3	4.60078E-3
Ternary	x(Nb)	7.02208E-2	7.68167E-2	8.33396E-2	1.08464E-1	1.3770407	1.6573519
	x(Al)	3.69481E-2	3.52004E-2	3.35163E-2	2.76009E-2	2.22268E-2	1.85501E-2
Phase	γ	8.74894E-1	8.47409E-1	8.19784E-1	7.07625E-1	5.61888E-1	4.07322E-1
	γ'	7.19936E-2	6.11267E-2	5.10207E-2	2.03855E-2	6.64289E-3	1.48702E-2
	γ"	5.31125E-2	9.14642E-2	1.29195E-1	2.71990E-1	4.31469E-1	5.77808E-1

Gibbs free energies of the four phases (γ, δ, γ', γ" phases) at T = 740°C were obtained from the TCNI8 database in the ThermoCalc for the Ni-Al-Nb system. A Python script was used to calculate the least-squares fit of the results to a quadratic equation of the form

$$G^p = A_1^p\left(x(Al) - A_4^p\right) + A_2^p\left(x(Nb) - A_5^p\right) + A_3^p \qquad [1]$$

where G^p is the Gibbs free energy of a phase p and A_1 to A_5 are the corresponding fitting parameters for phase, p. The script reads the data from ThermoCalc within the ranges $0 \leq$ x(Al) and x(Nb) ≤ 0.25, and returns the fitting parameters, which are listed in Table 4. The relative error of the fitting energy surfaces with respect to ThermoCalc data are lower than 10%. The fitting parameters were used in some of the early simulation to demonstrate the phase morphologies and equilibrium concentrations of the precipitate phases in 718. However, later simulations relied on the use of the Ni-Fe-Nb ternary because: (a) the Laves phase present in the as-built AM microstructure of 718 cannot be represented in a Ni-Al-Nb system as it

is thermodynamically unstable in this system and (b) the solidification range of Ni-Al-Nb alloy cannot match the equilibrium solidification range of alloy 718. The thermodynamic data generation for these two cases are shown next for the Ni-Fe-Nb model ternary system.

Table 4. Fitting parameters for Ni-Al-Nb system at 74

Phase	A_1	A_2	A_3	A_4	A_5
γ	182665	237617	-96148	0.44	0.24
γ'	110158	111036	-137130	0.75	0.51
γ"	212772	54356	-142815	0.48	1.0
δ	136834	139520	-125032	0.58	0.52

2.2.2 Ni-Fe-Nb

2.2.2.1 Ni-Fe-Nb free energy surfaces for Laves representation: We consider the dissolution of the Laves phase within the γ matrix. For the homogenization heat treatment, the temperature of T = 1100°C is typically used. Hence, we consider the temperature to obtain the Gibbs free energies of the γ matrix and Laves phases within the ranges of $0 \leq x(Fe)$ and $x(Nb) \leq 0.4$ using the TCNI8 database in ThermoCalc. As we have shown in the previous section, the ThermoCalc data were fitted to the quadratic equation of the form

$$G^p = B_1^p\left(x(Fe) - B_4^p\right) + B_2^p\left(x(Nb) - B_5^p\right) + B_3^p \quad [2]$$

The fit parameters are listed in Table 5.

Table 5. The fitting parameters for the matrix and Laves phase for the Fe-Nb-Ni system at T = 1100°C

Phase	B_1	B_2	B_3	B_4	B_5
γ	50121.2092	152659.0996	-91376.5576	0.19	0.28
Laves	44590.1461	105692.4264	-98243.1839	0.32	0.49

After the homogenization step, an additional heat treatment process is followed to nucleate and grow beneficial precipitates. For this annealing step, the target is to maximize the growth of beneficial γ" precipitates and minimize the δ growth in a matrix containing remnant Laves phase as it partially dissolves during the homogenization step at 1100°C. Two fixed temperatures were targeted, one for demonstrating the growth of the γ" at 650°C and another for demonstrating the growth of the δ phase at 830°C which is above the γ" solvus. These simulations were initiated from the previous simulation microstructure at T = 1100°C, when the Laves phase is not completely dissolved. Hence, Gibbs free energies of γ" and δ phases were obtained using ThermoCalc. At T = 650°C, the energy data were obtained within the ranges of $0.05 \leq x(Fe)$ and $x(Nb) \leq 0.4$ for the γ matrix and Laves phases, and $0.05 \leq x(Fe)$ and $x(Nb) \leq 0.35$ for the γ" phase. At T = 830°C, energy data were calculated within the ranges of $0.1 \leq x(Fe)$ and $x(Nb) \leq 0.35$ for the γ matrix and the δ phases, and $0.1 \leq x(Fe)$ and $x(Nb) \leq 0.4$ for the γ". Those energy values were fitted to the quadratic equation of the form in Eqn. 2 above using the python script. The estimated parameters are listed in Table 6 for T = 650°C, and Table 7 for T = 830°C.

Table 6. Fitting parameters for phases co-existing T = 650°C for the Ni-Fe-Nb Alloy

Phase	B_1	B_2	B_3	B_4	B_5
γ	34188.5206	132875.3921	-59166.5592	0.03	0.29
γ"	42799.8361	599253.5898	-61232.1940	0.0	0.25
Laves	25639.6012	105885.4264	-65907.8274	0.27	0.52

Table 7. Fitting parameters for phases coexisting at T = 830°C for the Fe-Nb-Ni system

Phase	B_1	B_2	B_3	B_4	B_5
γ	36182.5071	133853.5084	-71206.1792	0.07	0.28
δ	36132.1877	382808.9975	-74998.7843	0.0	0.26
Laves	25820.4771	135864.0192	-76581.2384	0.29	0.45

2.2.2.2 Ni-Fe-Nb alloy for solid-state precipitation with matching solidification range for alloy 718: Finally, the feasibility of expressing the composition of alloy IN718 using the Ni-Fe-Nb system to satisfy both the solidification range of alloy 718 as well as the volume fractions of various phases at different annealing temperatures was explored using the following approach. Initially, the solidification range for the nominal composition of IN718 was calculated using ThermoCalc. Then, the Ni-Fe-Nb alloy that satisfied the volume fractions of γ" and δ phases in IN718 at an annealing temperature of 800°C and the solidification range of IN718 was calculated through a trial-and-error procedure. The composition of Ni-0.500679Fe-0.0535985Nb was found to satisfy both of these conditions at 800°C. Subsequently, the error on the volume fractions of γ" and δ phases at different annealing temperatures ranging from 600°C to 850°C was calculated based on the above ternary composition. Table 8 lists the error data. The errors range from about 2% for 800°C to about 18% for 600°C. The approach shows that in order to accurately represent the precipitation in IN718, it may be necessary to consider quaternary or even quinary alloys. However, for the purposes of this project the model alloys were limited to ternary alloys.

Table 8. Comparison of volume fractions of phases between IN718 and Ni-Fe-Nb

Temperature $°C$	Volume fraction of γ"			Volume fraction of δ		
	IN718	Ternary	Error [%]	IN718	Ternary	Error [%]
600	0.17956109	0.18632795	3.77	0.18587858	0.19024737	2.35
650	0.17460229	0.17597681	0.78	0.182595	0.18118491	0.77
700	0.16689317	0.1605981	3.77	0.17755955	0.16768287	5.56
750	0.15530331	0.13875036	10.66	0.17007623	0.14851488	12.68
800	0.13828919	0.10891715	21.24	0.15924199	0.1224287	23.12
850	0.11373661	6.957460E-2	38.83	0.14387935	8.820682E-2	38.69

The free energy parameters for the various precipitates corresponding Eqn. 2 at different temperatures used as input to MEUMAPPS-SS simulations using Ni-Fe-Nb ternary are shown in Tables 9-12.

Table 9. Free energy surfaces for the model Ni-Fe-Nb alloy (γ matrix)

Temperature	B_1	B_2	B_3	B_4	B_5
600°C	40827.8461	135504.7324	-49994.4052	0.3	0.2
650°C	40045.7641	135630.2902	-53442.6298	0.3	0.2
700°C	39283.2839	135549.5193	-56974.8554	0.3	0.2
750°C	38533.6567	135312.0572	-60587.6773	0.3	0.2
800°C	37792.7512	134947.9971	-64278.0531	0.3	0.2
850°C	37057.9704	134477.9375	-68043.2665	0.3	0.2
1100°C	33430.3561	130918.5727	-87913.2778	0.3	0.2

Table 10. Free energy surfaces for the model Ni-Fe-Nb alloy (γ")

Temperature	B_1	B_2	B_3	B_4	B_5
600°C	121233.8730	925046.5568	-61363.8689	0.0	0.25
650°C	129132.8456	905049.2209	-64112.7428	0.01	0.25
700°C	110075.0334	885054.2592	-66986.5780	0.01	0.25
750°C	90996.4247	865061.7907	-69939.1083	0.01	0.25
800°C	93941.1148	845072.1153	-72955.7482	0.02	0.25
850°C	70443.6530	825085.2694	-76063.1575	0.02	0.25
1100°C	152694.6467	1063600.8359	-94064.7842	0.05	0.26

Table 11. Free energy surfaces for the model Ni-Fe-Nb alloy (δ)

Temperature	B_1	B_2	B_3	B_4	B_5
600°C	66034.0347	680297.3704	-62402.5126	0.0	0.25
650°C	66186.5129	662542.0568	-65183.8644	0.01	0.25
700°C	49759.3752	644644.8117	-68066.4595	0.01	0.25
750°C	33176.4223	626607.9745	-71028.0178	0.01	0.25
800°C	26419.7991	608436.7567	-74071.7119	0.02	0.25
850°C	5563.6039	590138.9375	-77187.9777	0.02	0.25
1100°C	170354.7754	497134.1788	-94122.8848	0.05	0.25

Table 12. Free energy surfaces for the model Ni-Fe-Nb alloy (Laves)

Temperature	B_1	B_2	B_3	B_4	B_5
600°C	28592.7834	210784.5882	-56657.1862	0.3	0.33
650°C	28717.7789	207902.7030	-59996.6577	0.3	0.33
700°C	28831.0511	205001.9810	-63418.8564	0.3	0.33
750°C	28933.8945	202080.3555	-66920.5234	0.3	0.33
800°C	29027.2380	199136.1554	-70498.7265	0.3	0.33
850°C	29112.0383	196168.0042	-74150.8275	0.3	0.33
1100°C	29089.2394	170764.1692	-93586.2161	0.3	0.34

2.3 TASK 3: TERNARY SYSTEM MODEL FOR SOLID-STATE TRANSFORMATIONS

Objective: The objective of this task is to demonstrate test cases of solid-state precipitation in model ternary alloys described in Task 2, to demonstrate multiple-phase precipitation.

Progress: The progress achieved is discussed along two subtask activities: (a) Modification of MEUMAPPS-SS to handle multiple phase precipitation, and (2) Demonstration simulations that show the capability of MEUMAPPS-SS to handle co-precipitation of phases involved in IN718.

2.3.1 Modification of MEUMAPPS-SS

The existing single-phase version of MEUMAPPS-SS was based on the phase field model proposed for the solidification of binary alloys by Kim, Kim, and Suzuki (KKS) [1]. The basic assumption in the model is that the diffuse interface across two phases is made up of varying volume fractions of the solid and liquid phases whose compositions are such that the chemical potentials of the solute(s) are the same in the two phases. The single-phase KKS model was extended to multiple phases and multiple crystallographic variants of the same phase based on an approach presented by Zhou et al. [2]. Accordingly, the total chemical energy of the system consisting of the γ matrix and the different variants of the γ", γ', and δ phases is defined as

$$G = \left[1 - \sum_{p=1}^{16} h(\phi_p)\right] G^{\gamma} + h(\phi_1) G^{\gamma'} \sum_{p=2}^{4} h(\phi_p) G^{\gamma''} + \sum_{p=5}^{16} h(\phi_p) G^{\delta} \quad [3]$$

where h is an interpolating polynomial for the free energy given by

$$h(\phi) = \phi^3(6\phi^2 - 15\phi + 10) \quad [4]$$

The total interfacial energy is given by

$$G^{int} = \omega^{\gamma'} \phi_1^2 (1 - \phi_1)^2 + \omega^{\gamma''} \sum_{p=2}^{4} \phi_p^2 \left(1 - \phi_p\right)^2 + \omega^{\delta} \sum_{p=5}^{16} \phi_p^2 \left(1 - \phi_p\right)^2 + \sum_{i=1}^{16} \sum_{j \neq i}^{16} \phi_i^2 \phi_j^2 \quad [5]$$

where the first term on the right-hand side is the interfacial energy between the single variant of γ' and the matrix, the second term is the interfacial energy between each of the 3 variants of γ" and the matrix, the third term is the interfacial energy between each of the 12 variants of δ and the matrix, and the last term is the interfacial energy between the different variants of the precipitating phases. A gradient energy is used to account for the energy penalty due to gradients in ϕ given by

$$G^{Grad} = 0.5 \sum_{p=1}^{16} \nabla \phi_p^T \kappa^p \nabla \phi_p \quad [6]$$

where κ is an anisotropic gradient coefficient. The eigenstrain associated with precipitation, results in an elastic energy term given by [3]

$$G^{Elas} = \sum_{p=1}^{n} h(\phi_p) \frac{1}{2} \epsilon_{ij}^{el,p} : C_{ijkl}^{p} \epsilon_{ij}^{el,p} : \epsilon_{ij}^{el,p} + \left(1 - \sum_{p=1}^{n} h(\phi_p)\right) \epsilon_{ij}^{el,m} : C_{ijkl}^{m} : \epsilon_{kl}^{el,m} \quad [7]$$

where ϵ is the total elastic strain given by

$$\epsilon_{kl}^{el} = \overline{\epsilon_{kl}} + \frac{1}{2}\left[\frac{\partial u_k}{\partial r_l} + \frac{\partial u_l}{\partial r_k}\right] - \epsilon_{kl}^{*} \quad [8]$$

where $\overline{\epsilon_{kl}}$ is the mean strain, the second term on the right-hand side is the lattice inhomogeneous strain, and ϵ_{kl}^{*} is the eigenstrain. The elastic strain energy calculation explicitly considers the elastic constants of the matrix and the individual precipitates based on their crystal structure. The eigenstrain matrices prescribed in the local frame of the crystal are rotated to the computational frame. Similar rotations are also performed for the gradient coefficient terms based on the crystal symmetry and the misorientation between the local crystal frame and the computational frame. The evolution equations solved are the time-dependent Ginzburg-Landau (TDGL) equation and the diffusion equation. The TDGL is given by

$$\frac{\partial \phi_p}{\partial t} = -\frac{\mathrm{L}}{\widetilde{N}} \sum_{p \neq q}^{\widetilde{N}} \left(\frac{\delta G}{\delta \phi_p} - \frac{\delta G}{\delta \phi_q} \right) \quad [9]$$

where L is the phase field mobility, and $\widetilde{N}$ is the total number of variants that co-exist at any mesh point, and the δ on the right-hand side refer to functional derivatives. The above formulation of the TDGL satisfies the constraint that the sum of the ϕs at any point satisfies the condition $\sum_{p=1}^{N+1} \phi_p = 1$ at every mesh point. The diffusion equation is given by

$$\frac{\partial C_{Fe(Al),Nb}}{\partial t} = \nabla . M_{Fe(Al),Nb} \nabla \mu_{Fe(Al),Nb} \quad [10]$$

where M is the mobility of Fe (or Al in Ni-Al-Nb system) and Nb and μ-s represent the chemical potentials of the species in each phase. The KKS formulation requires the calculation of the Fe (or Al) and Nb compositions at the various diffuse interfaces between phases using the equal chemical potential assumption, $\mu_{Nb} = \frac{\partial G^{\gamma}}{\partial C_{Fe(Al)}^{\gamma}}$. This requires solution to M x N simultaneous equations where M is the number of solutes, and N is the number of phases in the system. Representing the chemical free energies in the form quadratic equations described in Task 2 leads to a system of linear equations. The evolution equations are solved using a semi-implicit Fourier spectral technique, which is well established in the literature [4]. Parallel implementation of MEUMAPPS-SS on the ORNL supercomputer Summit was accomplished via Message Passing Interface and the use of a parallel three-Dimensional fast Fourier transforms (P3DFFT) package[5]. MEUMAPPS-SS shows excellent scaling over thousands of CPU cores in Summit [6].

2.3.2 Demonstration Simulations Using the Ternary, Multi-phase Model

Typical results obtained using the above free-energy surfaces are shown in the subsequent paragraphs.

2.3.2.1 Prediction of precipitate morphology and composition

The Ni-Al-Nb pseudo-ternary was used to simulate the equilibrium shapes of the γ' and δ morphologies as well as the partitioning of Al and Nb within the phases. The simulations captured the expected morphologies of the phases and their compositions as shown in Figure 5. The shape of the γ' phase is cuboidal / spherical, consistent with an elastic strain of 0.3% along the orthogonal directions. The shape of the δ phase is based on the stress-free transformation strain matrix given in Zhou et al. [1]. It was assumed that the δ phase nucleated intragranularly as a coherent phase. The results were presented at the U.S. National Congress on Computational Mechanics (USNCCM-15) held at Austin, Texas, in July 2019 [7]. As it will be shown later, it is necessary to alter the magnitudes of the transformation strains associated with the δ phase in order to capture the experimentally observed plate-like morphology for the intragranular precipitates.

2.3.2.2 Effect of Laves phase dissolution on precipitation of desirable phases

Initial results of Laves dissolution in IN718 and precipitation of δ phase and γ" phase in the Nb-rich regions surrounding the dissolving Laves phase were obtained using the Ni-Fe-Nb model ternary using the thermodynamic data shown earlier as input to MEUMAPPS-SS. The results were presented by Younggil Song, post-doctoral fellow at the Oak Ridge National Laboratory (currently at the Lawrence Livermore National Laboratory) working on the project, at The Minerals, Metals and Materials Society (TMS) Annual Conference held in San Diego, California in February 2020 [8]. Initially, Laves phase particles were introduced as spheres in a simulation domain of 256 x 256 x 256 mesh points. The initial concentration of Nb within the Laves phase was set as 0.316 (mole fraction) while the average Nb composition of the matrix alloy was 0.1. The dissolution of the Laves phase was simulated at 1100°C . Simulations showed the formation of Nb-rich regions surrounding the dissolving Laves phase in agreement with the alloy thermodynamics.

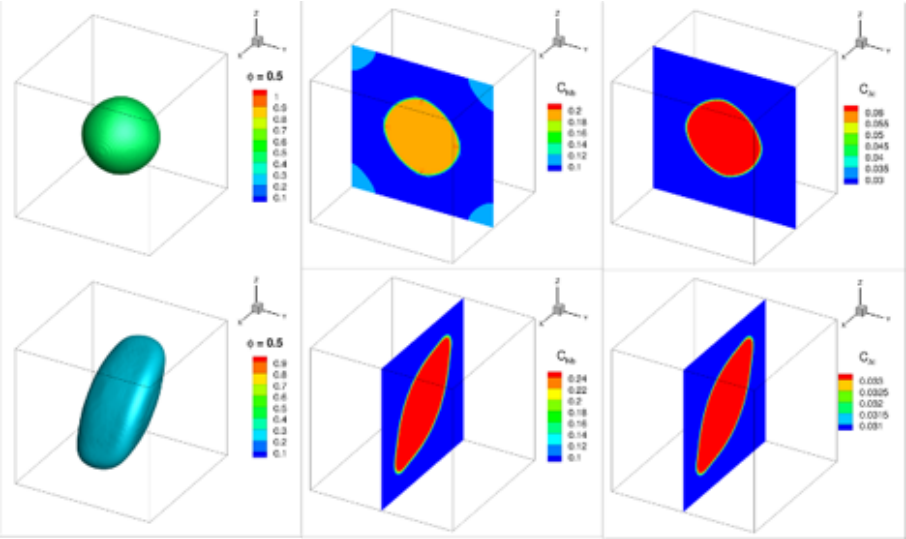

Figure 5. Morphology and composition of γ' phase (top row) and the δ phase (bottom row).

The initial domain and the concentrations of Fe and Nb around the dissolving Laves phase are shown in Figure 6. Growth of δ phase was simulated at 83. Spherical nuclei were introduced randomly within the matrix that contained the Nb-enriched regions around the Laves phase. The nuclei included all 12 crystallographic variants of the δ phase. The simulations showed that the nuclei that were present in the Nb-enriched region grew to become supercritical and showed the expected disc shaped morphology while the nuclei in low-Nb regions dissolved. The evolution of the δ nuclei is shown in Figure 7. The evolution of the γ" phase was simulated at 650°C using a similar procedure, as shown in Figure 8. In the case of γ" there are three crystallographic variants, and all three variants were included in the simulations. The simulations captured the expected disc shaped morphology of the γ" phase in the Nb-enriched zones while the nuclei disappeared in the Nb-lean regions, as shown in Figure 8, in agreement with the alloy thermodynamics. These simulations also showed the ability of the phase field simulations to handle multiple crystallographic variants of the precipitating phases.

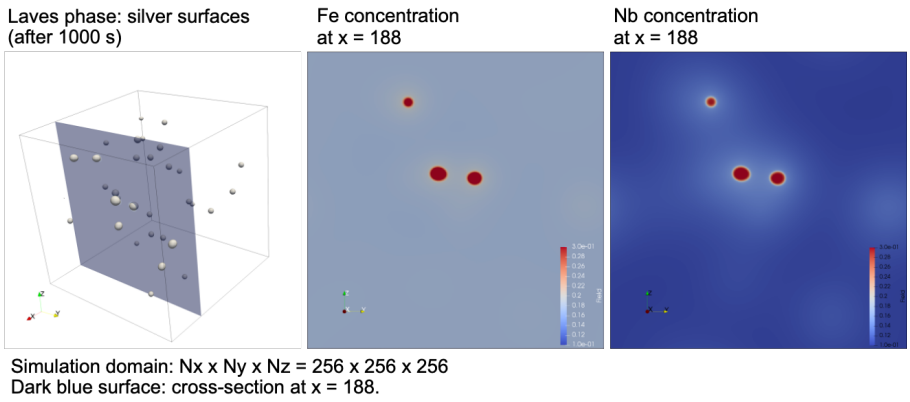

Figure 6. MEUMAPPS-SS simulations of Laves phase (silver, left) dissolution at 1100°C showing the enrichment of Fe(middle) and Nb(right) in the region surrounding the dissolving Laves phase.

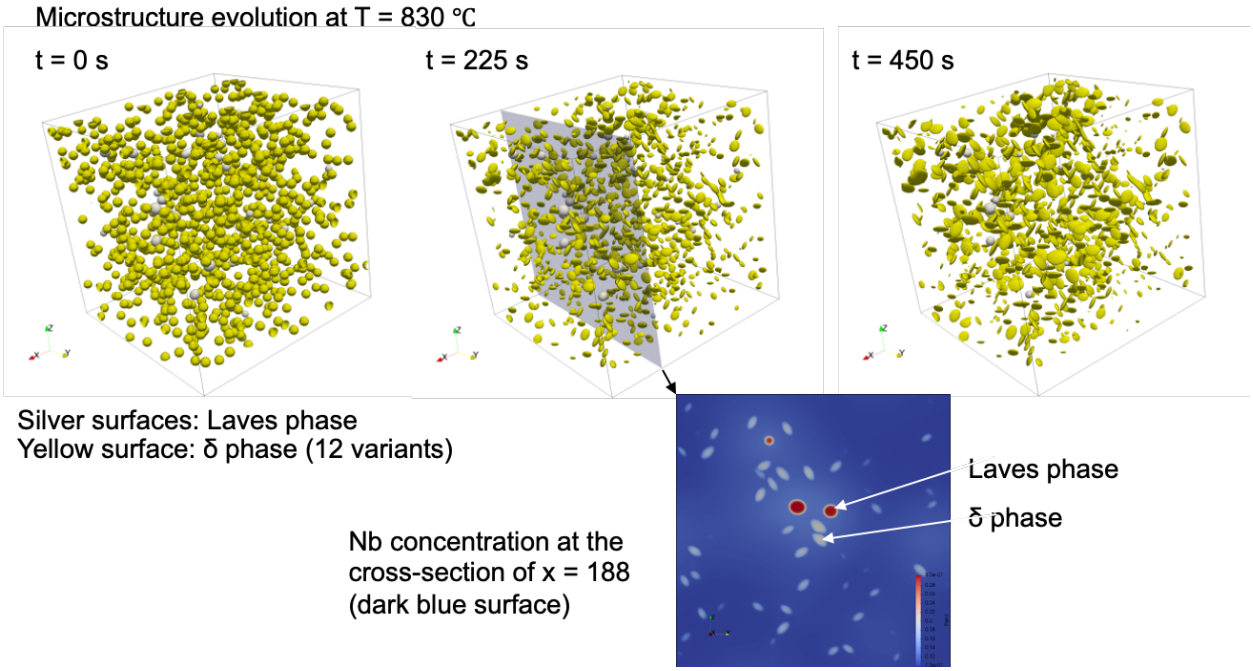

Figure 7. MEUMAPPS-SS simulations of the formation of the *δ* phase in the Nb-enriched regions of the dissolving Laves phase.

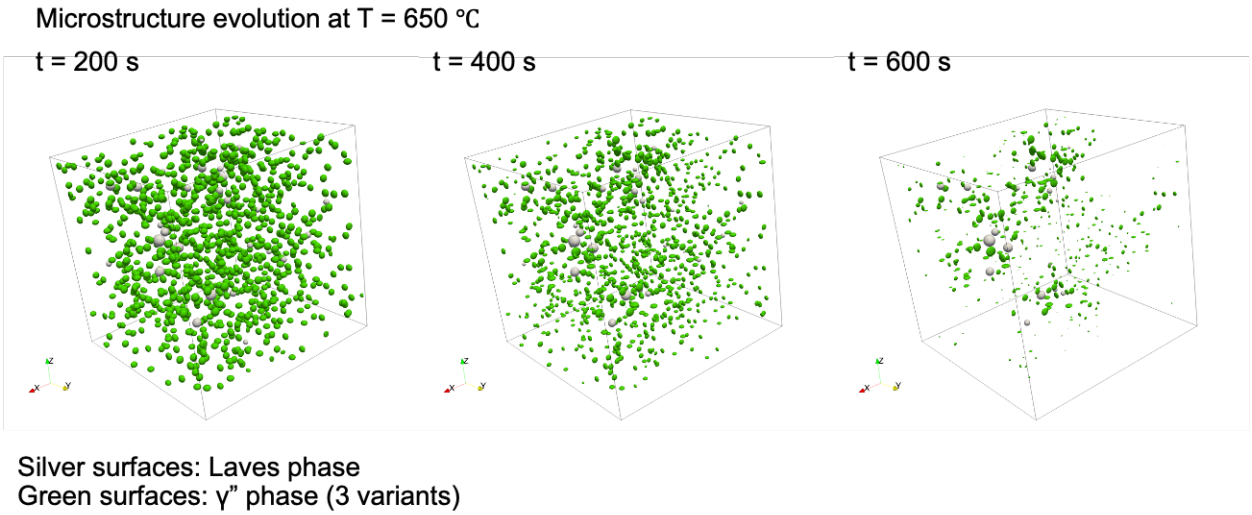

Figure 8. MEUMAPPS-SS simulations of the evolution of the γ'' phase at 650°C showing growth of the phase in the Nb-enriched regions surrounding the Laves phase.

2.3.2.3 Precipitation in a concentration gradient

The ability to simulate the effect of Nb concentration gradients on microstructure evolution gave rise to a more fundamental study that involved designing controlled Nb gradients and quantifying the effect of the gradients on the kinetics of evolution of the δ and γ'' phases. These studies led to a journal publication entitled, "Precipitate growth kinetics under inhomogeneous concentration fields using a phase-field model," in Physical Review Materials [9]. The main takeaway from the paper is that in the presence of a Nb concentration gradient, the growth rate of δ precipitates is higher than in a matrix of uniform average Nb concentration. The higher growth rate is a result of the higher local thermodynamic driving force at the interface between the solute-rich matrix and the δ interface. A phenomenological model was proposed to describe the diffusion-controlled growth kinetics of the δ phase under a solute concentration gradient. The initial Nb concentration gradient in the matrix was modified by partial homogenization of a linear concentration gradient as shown in Figure 9. The resulting δ phase precipitation after a 200s anneal at 850°C is shown in Figure 10. Precipitation was initiated by randomly placing spherical nuclei of a fixed size everywhere in the domain. Figure 11 shows the volume fraction of δ as a function of the distance in the z-direction of the domain.

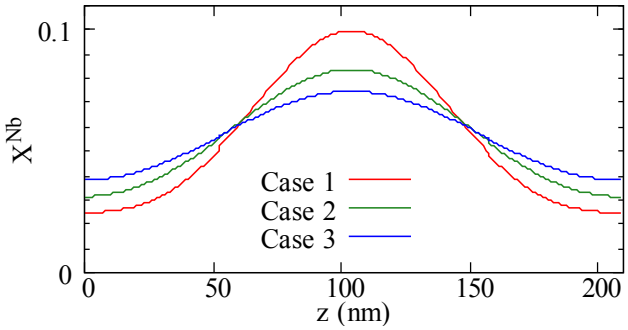

Figure 9. Initial Nb concentration in the simulation domain obtained through partial homogenization of a linear gradient symmetrically distributed along the z-direction.

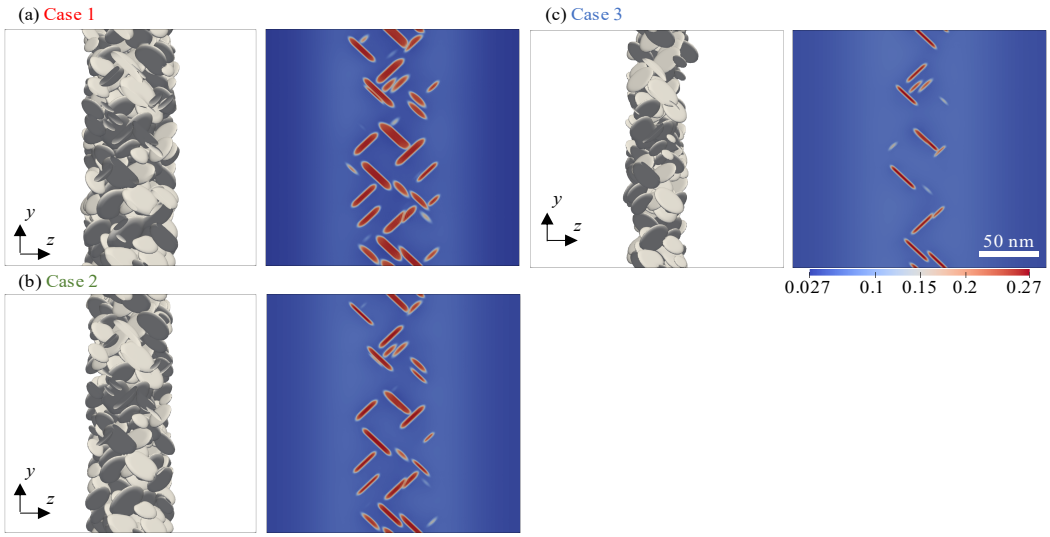

Figure 10. δ phase precipitation in the presence of the Nb-gradients shown in Figure 7a. The width of the precipitation zone is limited by the local Nb concentration

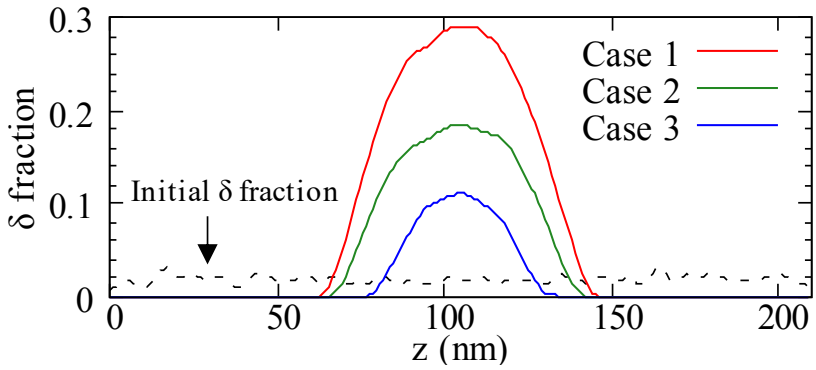

Figure 11. Volume fraction of δ phase as a function of distance. The initial volume fraction of the randomly placed nuclei is shown by the dotted line.

The local volume fraction of the δ phase is determined by the ability of the initially placed nuclei to survive and become supercritical as well as by the growth kinetics of the super-critical nuclei. The randomly placed nuclei all had the same radius of 1 nm. The critical nucleus size decreases with increasing Nb concentration because of the increasing thermodynamic driving force that reduces the activation energy for nucleation. Therefore, the width over which super-critical nuclei existed initially was the largest for case 3 because of the higher Nb concentration at larger distances from the center of the domain. However, the width of the δ precipitation zone is the largest for case 1, which indicates that the faster growth kinetics in regions with high Nb concentration controls the precipitation kinetics rather than the nucleation behavior.

In order to illustrate this point more clearly, simulations of growth kinetics of an isolated, single precipitate placed at the center of the domain with different initial Nb concentration gradients were performed. The growth kinetics in the presence of a concentration gradient was compared against kinetics in a matrix of uniform Nb concentration. Figure 8a shows the initial concentration profiles in the simulation domain. In addition to the uniform Nb concentration case, three different gradients were considered. These are shown as the shallow, moderate, and deep gradients in Figure 12a. The gradients

were designed such that the average concentration of the alloy is the same in three conditions and were equal to the uniform concentration case. A spherical δ nucleus was placed at the center of the domain with an order parameter of 1.0. The initial Fe and Nb concentrations of the nucleus were set to the equilibrium precipitate concentrations at the growth simulation temperature of 850°C. The growth rate (volume fraction) of the precipitate as a function of simulation time is shown in Figure 12b. It is clear that the growth rate is faster in all the gradient cases compared to the unform concentration case.

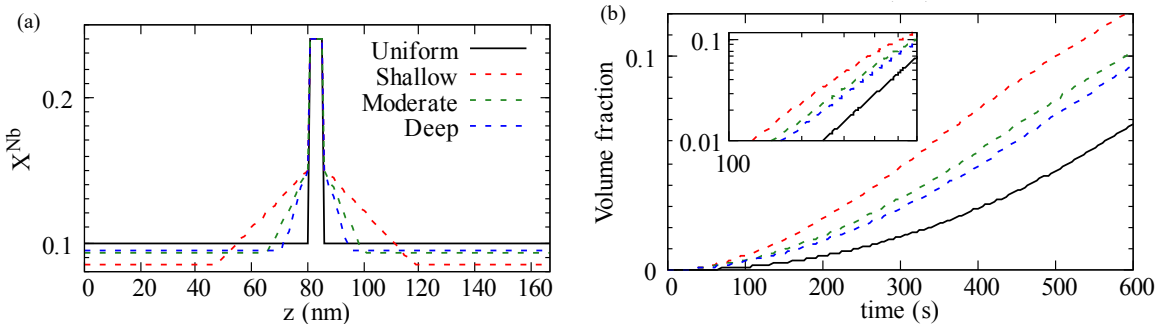

Figure 12. (a) Initial Nb concentration profiles, and (b) volume fraction of δ as a function of time at 850°C .

The δ precipitate exhibits a plate-like morphology, and hence we can describe its morphology based on its radius r within the (111) habit plane and thickness h orthogonal to the plane. Under steady-state conditions, the interfaces normal to r and h should satisfy diffusion-controlled growth dynamics based on the power law $g_0 t^{1/2}$, where g_0 is the growth constant. Including the elastic strain affects only the growth constant, and the power law exponent remains 1/2. Figure 13a shows the δ (silver) at t = 300 s.

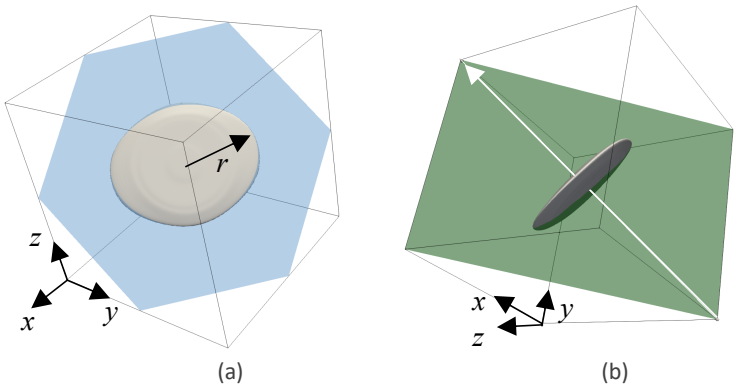

Figure 13. Disc shaped δ morphology showing the elliptical disc (a) on (111) habit plane and (b) the thickness normal to the habit plane.

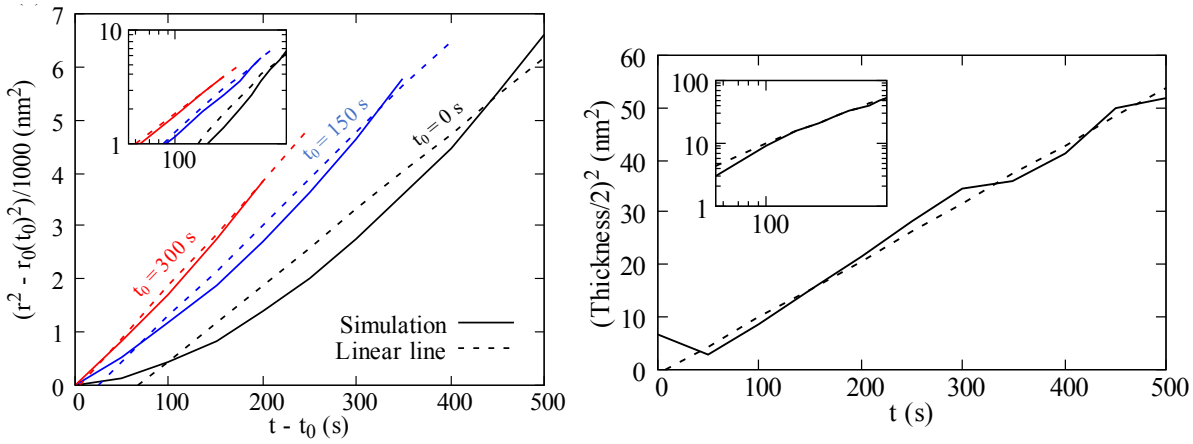

Figure 14. Left - $[r - r0\ (t_0)]^2$ of a δ precipitate, where r is the average radius and r0 is the radius using three reference times t_0 - $r_0(t_0)$ [nm] = 1.7 for t_0 = 0 s (black line), 29.2 for t0 = 150 s (blue line), and 52.4 for t_0 = 300 s (red line); Right – similar plot using the precipitate thickness normal to (111) plane

In Figure 13a, the δ shape as shown along the blue (111) plane is not a perfect ellipse because the shape is influenced by elastic energy and anisotropy in the interfacial energy. We interpolate interface positions (φ = 0.5) on the plane using the Paraview program. At t = 0 s, the program interpolated 21 positions. As the δ grows, it calculates more interface positions. For example, we obtained 907 positions for the δ in Figure 13a. We averaged the positions to compute the radius values for Figure 14a.

In Figure 14 (left), we plot $r^2 - r_0(t_0)^2$ as a function of time $t - t_0$ with a reference time t_0. We averaged the interface positions measured in the (111) habit plane to calculate the radius $r = r(t)$ at a time t. From the time when it reaches the steady state, the precipitate growth would show the power law growth and thus $r^2 - r_0(t_0)^2 \sim t - t_0$ [40, 41]. It is difficult to predict when the precipitate reaches the steady state, and hence we use three reference times, t_0 = 0 s, 150 s, and 300 s, and, at those times, the radii are $r_0(t_0)$ = 1.7, 29.2, and 52.4 nm, respectively. In the plot, solid lines are for simulation results and dashed lines are the linear fits. The insert in the figure is a log-log plot showing a linear fit.

The initial evolution of the δ phase occurs under the artificial nucleation conditions, and it takes some time for the conditions to reach a thermodynamically consistent state of growth. During this stage, the δ growth rate (black line) is faster than the linear slope expected from a purely diffusion-controlled growth. As time proceeds (blue and red lines), it approaches the diffusion-controlled growth limit. While we measure the radius only up to ~ 500 s since the δ grows out of the simulation box at longer simulation times, we expect the power law exponent to be satisfied (p = 1) under such conditions.

We averaged the measured thickness values of the δ in Figure 14 (right). The dashed line is the linear fit line using the simulation data (black solid line) from t = 50 s. The thickness, h, in the simulation shows steady-state growth according to $(0.5h)^2 \sim t$ (dashed line) from the beginning. We assume that, due to the slow thickness growth, the solute profiles quickly approach the steady state. Accordingly, we expect the diffusion-controlled growth to be reached fairly early in the process.

In the simulations, the δ precipitate grows as a noncircular plate. The volume during growth is mainly related to the mean radius of the plate, and its thickness. We have shown earlier that the thickness follows a diffusion-controlled growth with a growth exponent of roughly 0.5, while the growth exponent of the radius is higher at the initial transient stage during which thermodynamic consistency is being approached (Figure 14). Hence, the power law exponent S_g for the volume fraction given by,

$$V_f = V_0 t^{S_g} \quad [11]$$

is not 1.5 when evaluated from t=0. When we fit the simulation results for the uniform condition (black solid line in Figure 12b) to Eqn. (11), the power law exponent becomes $S_g = 2.15$ with $V_0 = 7.24 \times 10^{-8}$ (black dashed line). The higher growth rate in the presence of Nb gradient, with a higher Nb at the precipitate-matrix interface shown in Figure 12b, is probably due to the higher thermodynamic driving force associated with the higher Nb concentration. Accordingly, we can modify Eqn. (11) by introducing an additional contribution of F_R(t) as

$$V_f = F_R(t) V_0 t^{S_g} \quad [12]$$

to incorporate the effect of local solute concentration and the associated thermodynamic driving force on the volume fraction. The term F_R(t) would be related to the free energy and the diffusion dynamics. The chemical free energy is much higher than the elastic strain energy, and thus, provides the main contribution to the modification. The effect of Nb concentration on the driving force for growth is obtained through Eqn. (12). In addition, the precipitate growth would approach the growth kinetics under a uniform field as the solute field homogenizes. Therefore, the value approaches F_R(t) → 1 after a long time. Based on our simulation results, we suggest the following expression for F_R(t) to describe the δ growth under a solute gradient.

$$F_R(t) = \left(X_r^2 - b_0 \left(1 - exp\left(-{}^{t}/_{\tau} \right) \right) \right)^{S_f} \quad [13]$$

where the ratio $X_r^2 = {}^{X_{max}^{Nb}}/_{\bar{X}^{Nb}}$ is between the effective maximum and the average Nb concentrations, which are related to the free energy contribution. For the simulation with the shallow gradient, X_{max}^{Nb} = 0.15 and $\bar{X}^{Nb}$ = 0.1. The constant b_0 is determined $b_0 = X_r^2 - 1$, and hence the function F_R(t) =1 as time elapses. For the uniform case, the constants in the above equation become Xr = 1 and b_0 = 0, which leads to F_R(t) = 1. Then, Eqn. (13) is the same as the power law growth in Eqn. (11). We assume that the precipitate growth follows the same power law of $S_f = S_g = 2.15$ for the uniform case. The characteristic time τ is linked to the diffusion dynamics. We use the best-fit approximation to obtain τ within the simulation results before 400 s for the shallow gradient simulation (red solid line in Figure 14). The modified V_f in Eqn. (12) with the fitted τ = 501 s (red dashed line) agrees well with the simulation result.

2.3.2.4 Precipitation of multiple phases

The next step is to demonstrate the precipitation of multiple phases in a simulation domain with an initial concentration gradient. This is motivated by the experimental observation in post-AM heat treated alloy IN718 that shows that multiple phases such as (γ", γ', and δ phases and their variants) can form during direct aging. These simulations were performed using the Ni-Fe-Nb ternary as before, using initial Nb concentration gradients set up by the dissolution of the Laves phase. The co-precipitation of γ", and δ phases at 650°C and 850°C are shown in Figures 15a and 15b.

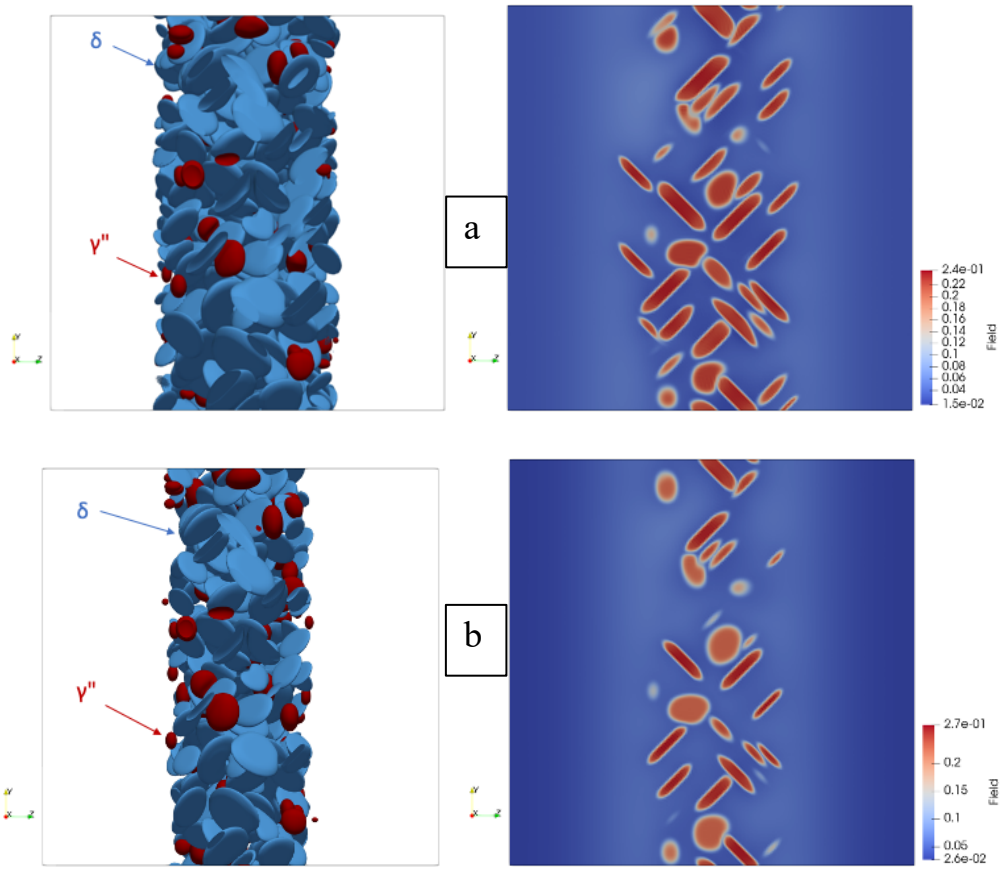

Figure 15. Simulation of co-precipitation of δ and phase in two different Nb concentration gradients. The simulations capture the preferential precipitation of δ and γ" phases in the Nb-enriched region corresponding to the interdendritic regions in an AM solidification microstructure. (a) 650°C and (b) 850°C .

The wavelength and extent of precipitation inside the Nb-enriched zone can be controlled through the design of the initial Nb gradient that can be achieved by varying the extent of homogenization subsequent to the dissolution of the Laves phase particles. Such functionally gradient materials are known to possess exceptional combination of strength and ductility compared to microstructures with uniform precipitation. The simulations indicate that a wider precipitation zone of γ" and δ is obtained a650°C than 850°C , indicating that at higher temperatures either the driving force for precipitation decreases for a given Nb concentration, or the occurrence of a lateral Nb flow during the aging treatment has an influence on the amount of precipitation. These factors have to be considered during the design of custom heat treatments based on direct aging. While the current phase field simulations have focused on precipitation inside the grains, in AM processed solidification microstructures containing dendritic / cellular structures, δ phase precipitates preferentially on the dendrite / cell boundaries that have the highest Nb content and the cell boundary that aids the nucleation. Examples of co-precipitation in post-AM heat treated IN 718 can be found in the recent literature. Figure 16 shows precipitation behavior in AM-built 718 after a post-AM heat treatments [10] solution treating at 980°C for 1 hr. δ phase precipitation is observed both at the solidification cell boundaries and in the intra-cellular regions as shown in Figure 16a. At a higher magnification of the cell boundary region shown in Figure 16b, co-precipitation of γ" and γ' is evident. The MEUMAPPS-SS simulations shown in Figure 15 qualitatively capture the co-precipitation in IN 718

during post AM heat treatment. The Ni-Fe-Nb ternary does not capture the formation of γ' due to the absence of Al and Ti that are the major constituents that partition to γ'.

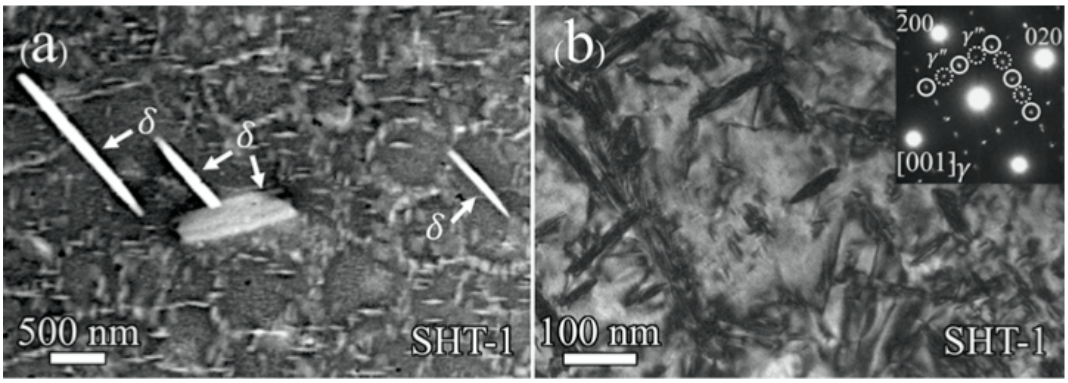

Figure 16. Co-precipitation of γ'', γ', and δ phases during post AM heat treatment of IN718 [10].

2.3.2.5 Precipitation on dislocations

Another important aspect of the microstructure during AM is the formation a dislocation substructure shown in Figure 17. It is interesting that the dislocation cell walls are aligned with the solidification cell boundaries that also have the highest solute content due to micro segregation. The nucleation kinetics are influenced both by the high solute content at the cell boundaries as well as by the heterogeneous nucleation due to the presence of cell boundary. The intercellular regions close to the cell boundary also have a sufficient segregation of solutes and contain a network of forest dislocations whose strain field may influence the phase selection during nucleation.

Experimentally, it has been observed that the dislocations act as preferential nucleation sites for γ'', γ'. In order to capture the effect of dislocation strain field on the nucleation of phases in 718, a simple dislocation model was introduced within MEUMAPPS-SS based on the approaches shown in the literature [11]. A pure edge dislocation was introduced on a (111) slip plane with a Burgers vector in the $(1\bar{1}0)$ direction. The strain field associated with the dislocation line was modeled as the eigenstrain of a precipitate. The eigenstrain due to the edge dislocation is given by $\varepsilon_{ij}^{dis} = \frac{b\otimes n+n\otimes b}{2d}$ where b is the Burger's vector, n is the slip plane normal, and d is the interplanar spacing of the (111) slip planes. A schematic of the dislocation model is shown in Figure 18.

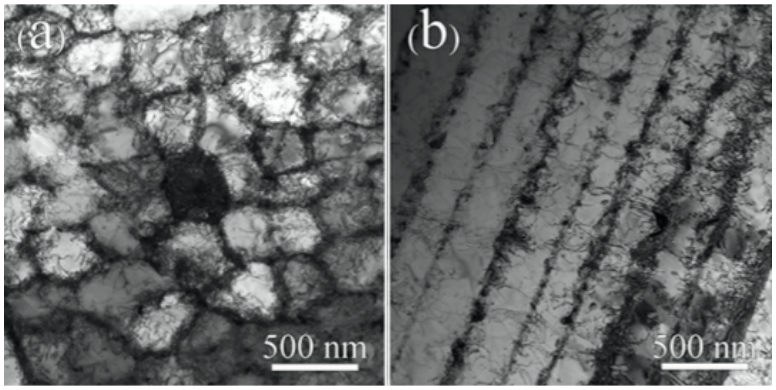

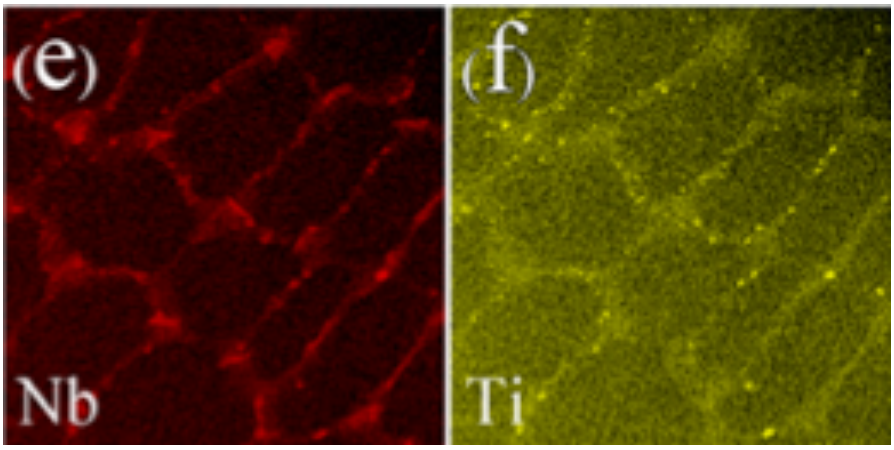

Figure 17. Microstructure of IN718 after LPBF AM process showing dislocation cell structure (top) and corresponding micro segregation of Nb and Ti to the cell boundaries [10].

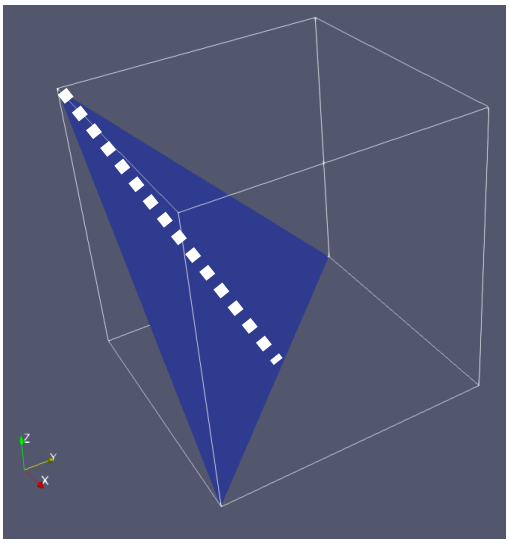

Figure 18. Schematic of the dislocation model used in MEUMAPPS-SS. The model shown here was also extended to multiple dislocations lines parallel to the line shown.

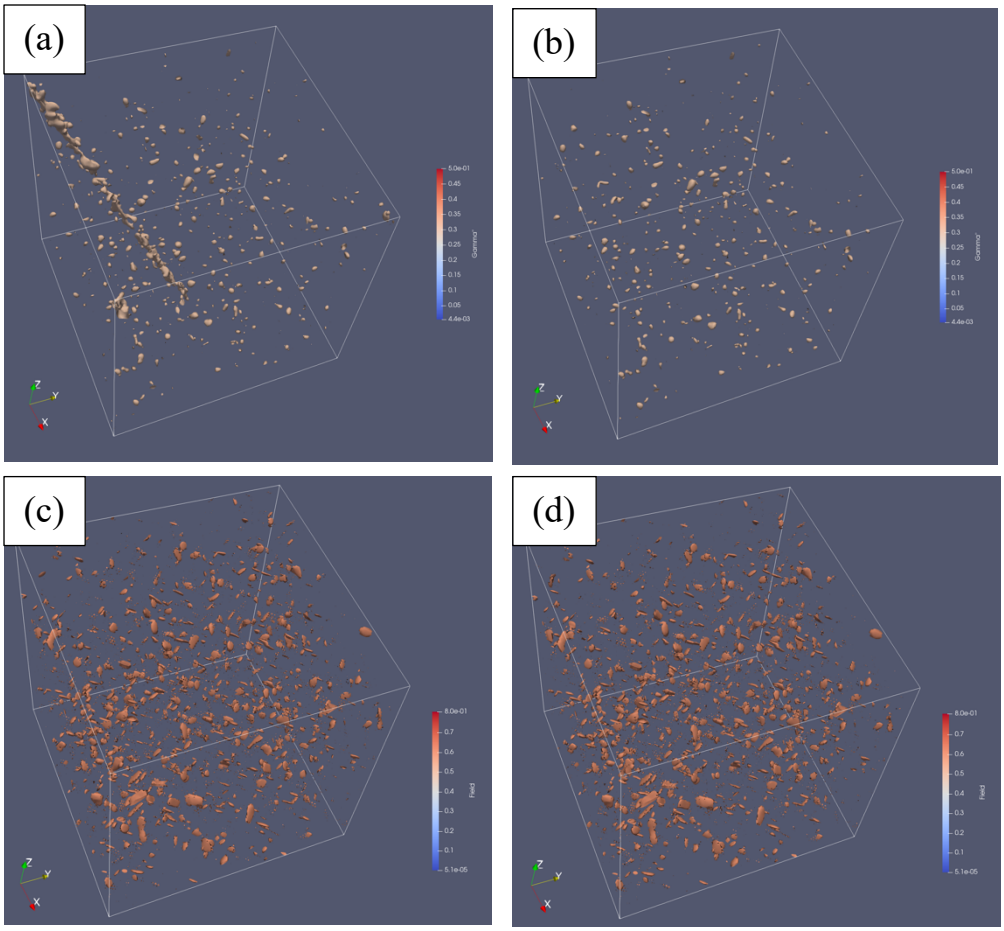

Figure 19. Nucleation of γ" in the presence of the strain field due to an edge dislocation line (a) and in the absence of a dislocation line (b). The dislocation strain field clearly promotes the preferential nucleation of γ". Dislocation strain field has no significant effect on the nucleation of the δ phase as shown in (c) with dislocation and (d) without dislocation.

The effect of the dislocation strain field on phase selection during post-AM annealing is shown in Figure 19. The alloy composition is Ni-0.379Fe-0.15Nb. The results shown in Figure 19 correspond to a short anneal of 30s at 750°C . The simulations were carried out in a domain of 126 x 126 x 126 mesh points with a resolution of 1 nm. Clearly, the dislocation strain field is seen to promote γ" in its vicinity while it has no effect on the δ phase precipitation.

2.4 TASK 4: MODELING AND VALIDATION WITH VARIABLE INITIAL MICROSTRUCTURE AND HEAT TREATMENT

Objective:

Progress: With the above base capabilities developed and demonstrated in MEUMAPPS-SS, parametric simulations were carried out by systematically varying the alloy composition and the heat treatment temperature to determine the effect of these parameters on the precipitation of phases. These simulations were performed using the Ni-Fe-Nb model ternary alloy. Since γ' does not form in this system due to the

absence of Al or Ti the competing phases that precipitate are only γ" and δ. Figure 20 shows the alloy and heat treatment parameters considered. These simulations assume that the Laves phase has been removed through a partial homogenization treatment. Therefore, the simulation cells only consist of the γ matrix initially. The Fe and Nb concentrations shown in Figure 20 are assumed to represent various locations in the interdendritic region with variable Nb content. In addition, simulations were also performed using simulation domains with an initial concentration gradient as well as domains with or without a dislocation line in order to assess the effect of the dislocation strain field on the phase selection during heat treatment.

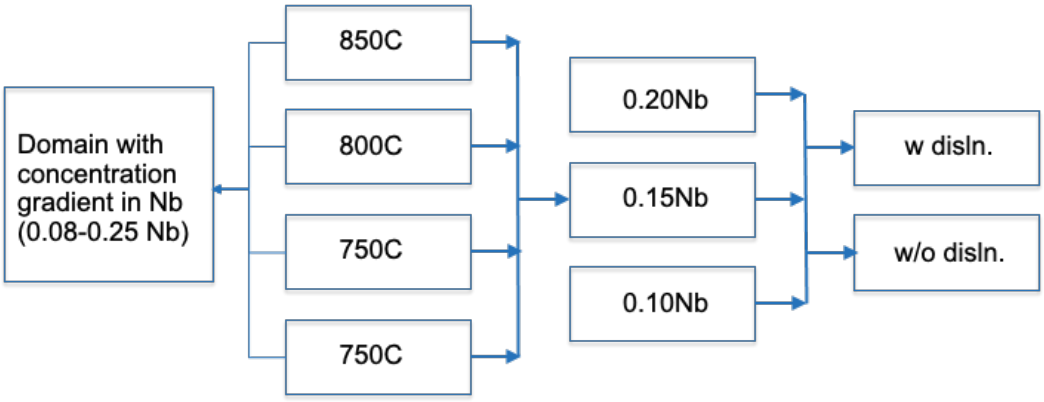

Figure 20. Schematic lay-out of the collection of parametric studies used for Task 4.

The collective layout of the parametric studies shown in Figure 20 shows that totally 24 different simulation conditions were tried out to quantify the effect of heat treatment temperature, alloy concentration and the dislocation strain field on the phases that form during annealing. The above simulations were carried out using a simulation domain of 126 x 126 x 126 points with a spacing of 1 nm using a time step of 5 x 10-3 s. The total heat treatment time was limited to 100s because the precipitation kinetics at these high Nb concentrations are known to be extremely fast. Nucleation was simulated using a Langevin noise causing a perturbation in the order parameters of the 3 γ" variants (variants 1-3) and the 12 δ variants (variants 4-15). The simulations indicated that for both of the conditions used, the δ variants dominated and prevailed over the γ" variants that formed at shorter nucleation times. The presence of the dislocation strain field appeared to stabilize the γ" variants for a longer time compared to the dislocation-free case. However, at longer simulation times the δ variants still prevailed. Preferential formation of γ" at the expense of the δ phase occurred only at a simulation temperature of 850°C , especially for low Nb concentrations. Summary of the nucleation kinetics and phase selections are shown in Figures 21-24. In Figures 21-24, the volume fraction is expressed as the sum of the squares of the order parameter of each variant in the domain divided by the total number of points in the domain.

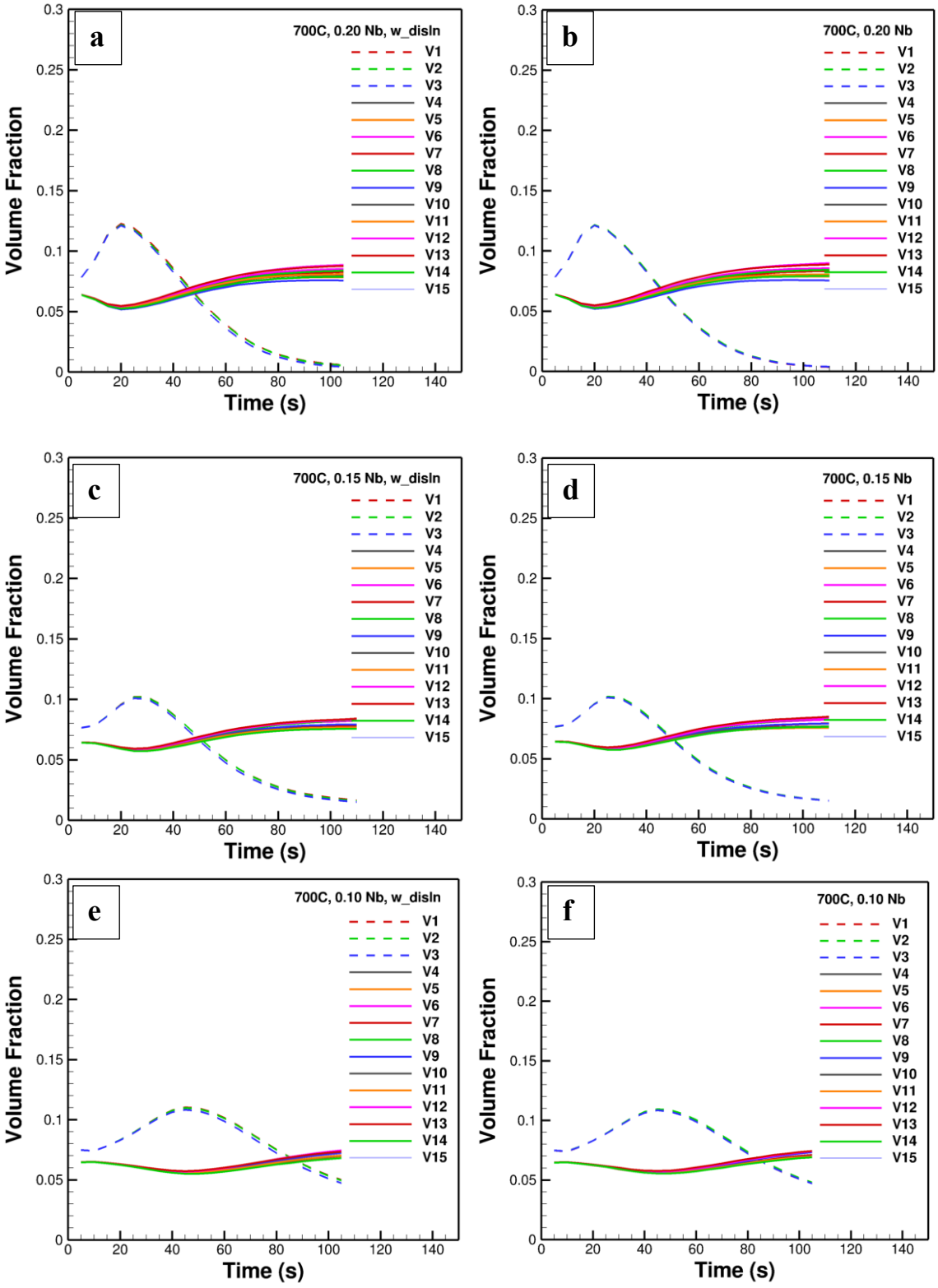

Figure 21. Relative nucleation and growth of γ" and δ variants at 700°C as a function of alloy composition and dislocation strain field.

The evolution of the γ" and δ variants with time at an annealing temperature of 700°C shown in Figure 21 shows that the final stable microstructure after an anneal of 140s consists mainly of the 12 δ variants with the γ" variants that tend to increase at early times are eventually consumed by the δ variants. In these simulations as well as in subsequent simulations, the nucleation was introduced as fluctuations in all the 15 order parameters consisting of the 3 variants of γ" and 12 variants of the δ phase. The lower Nb alloy consisting of 0.10 Nb tends to have a higher stability of the γ" variants to longer times, but they are ultimately taken over by the δ variants. This trend seems to be true for simulations with or without the presence of initial strain field due to the dislocation line. The same trend is also observed when the simulations were repeated for an annealing temperature of 750°C, as seen by comparing the results in Figures 22 and 23. The fact that the δ volume fraction begins to increase after an initial increase in the γ" fraction indicates that the growth of δ seems to be favored by the presence of γ" either due to heterogeneous nucleation on γ" or due to the favorable influence of the strain fields developed by the γ" variants. The relative volume fraction of δ / γ" seems to be a function of the Nb content in the alloy, the δ being the most stable in the higher 0.20 Nb alloy and least stable in the 0.10 Nb alloy. These results indicate that the nucleation of the δ phase is promoted by the initial presence of the γ" phase that nucleates more easily because of the lower activation energy. However, once stable δ nuclei are formed it takes over completely because of the increased thermodynamic driving force, and therefore consumes the γ" phase. This trend is exhibited both for the $700°C$, $750°C$, and $800°C$ anneals with or without dislocation strain field shown in Figures 21-23.

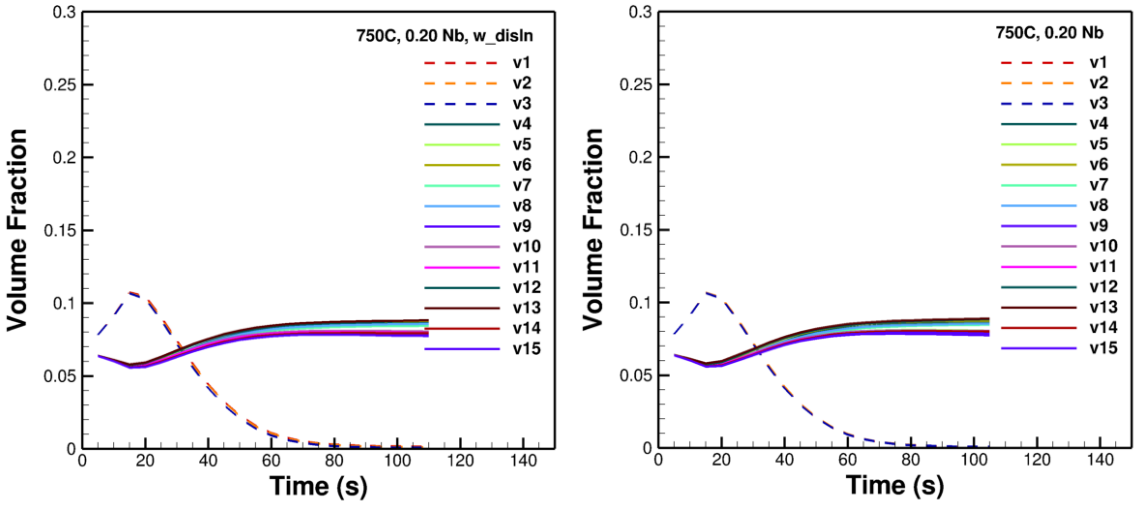

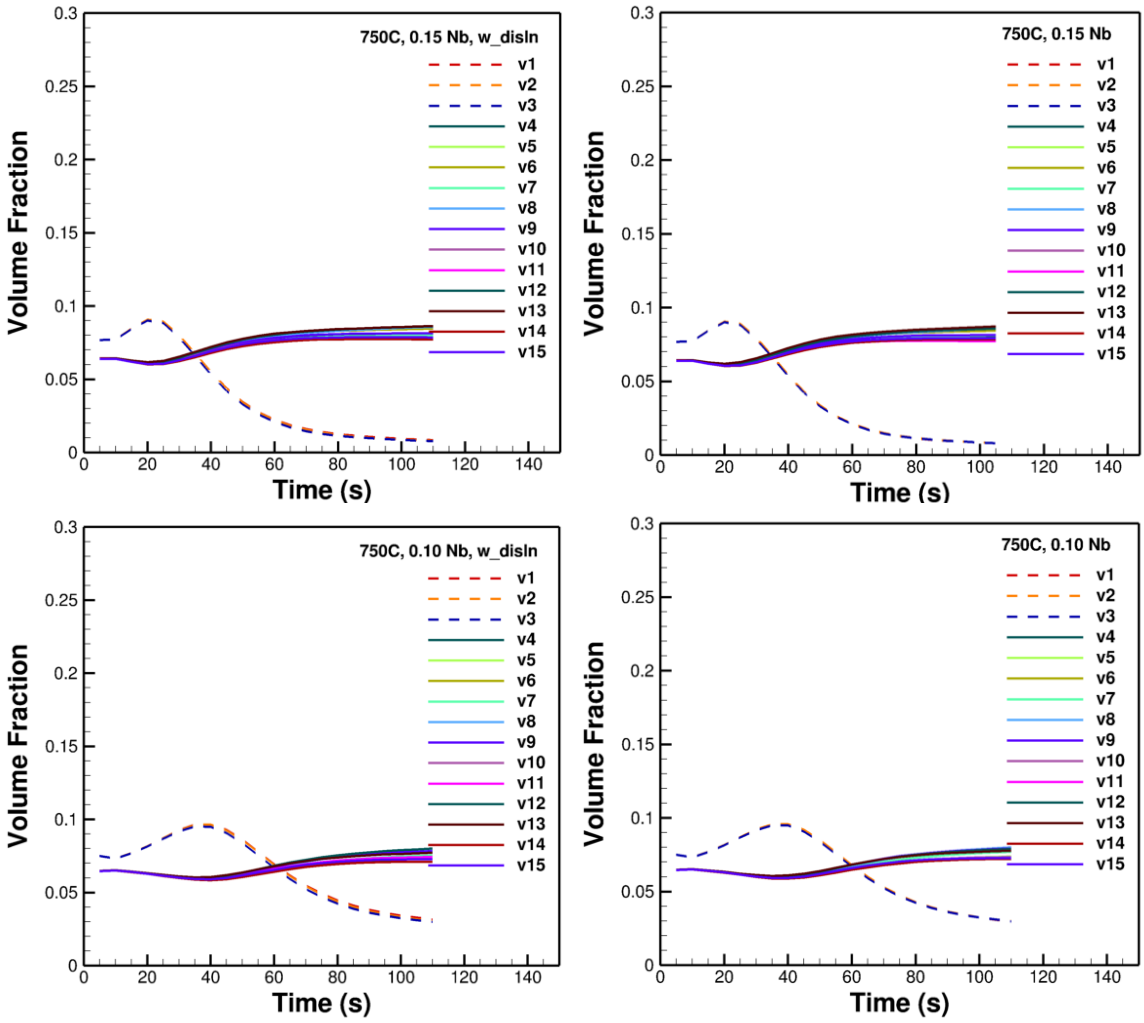

Figure 22. Relative nucleation and growth of γ" and δ variants at 750°C as a function of alloy composition and dislocation strain field.

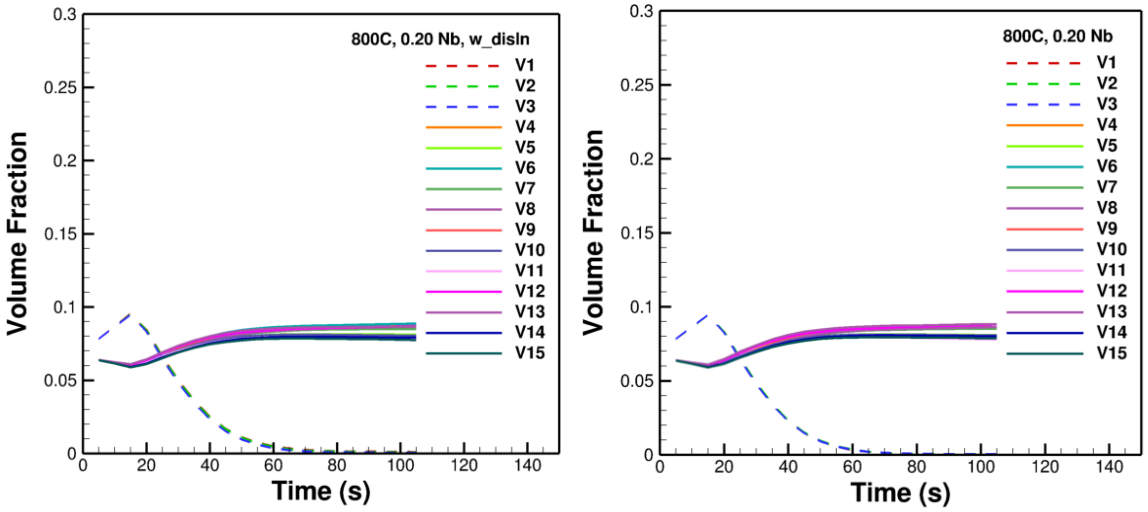

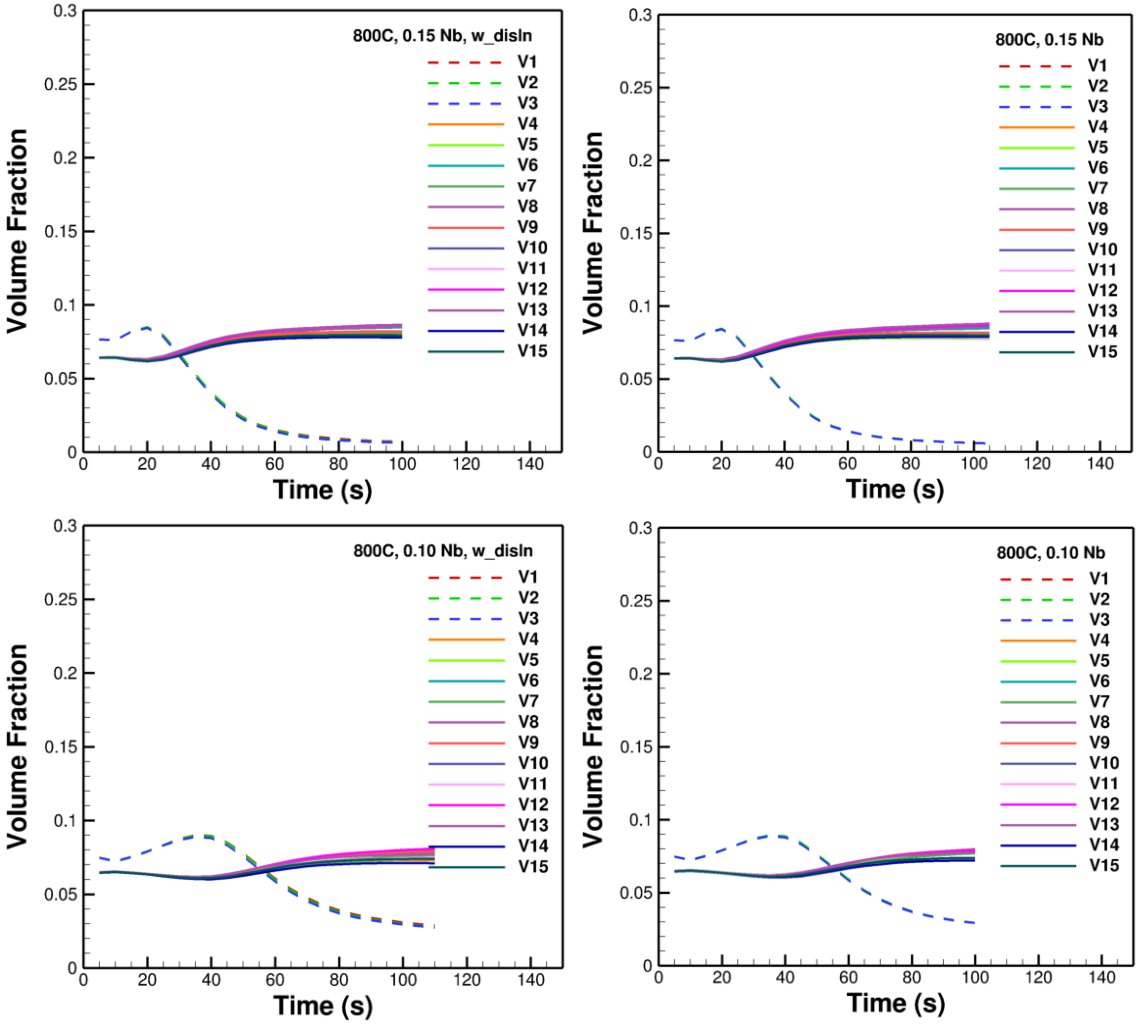

Figure 23. Relative nucleation and growth of γ" and δ variants at 800°C as a function of alloy composition and dislocation strain field.

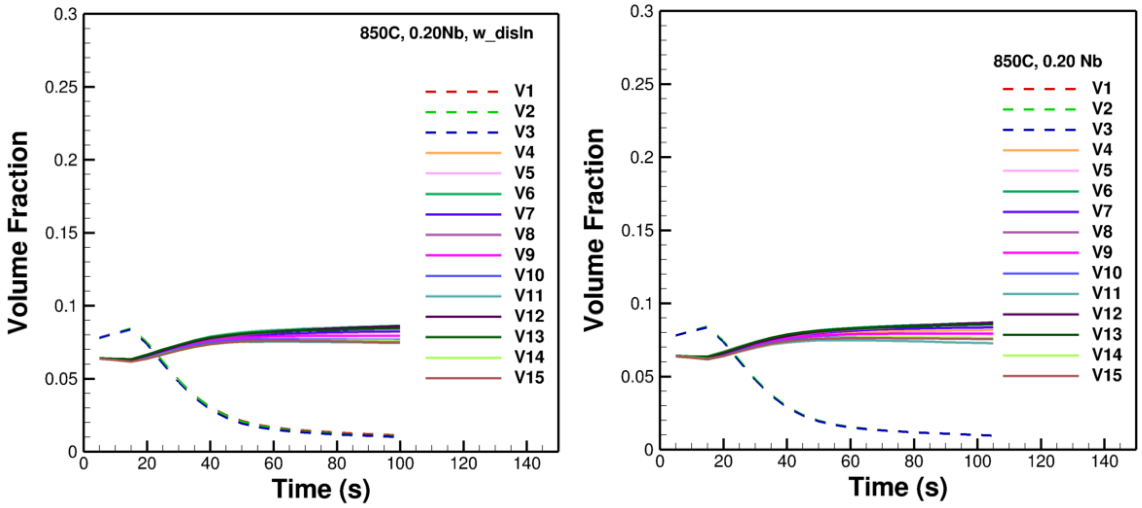

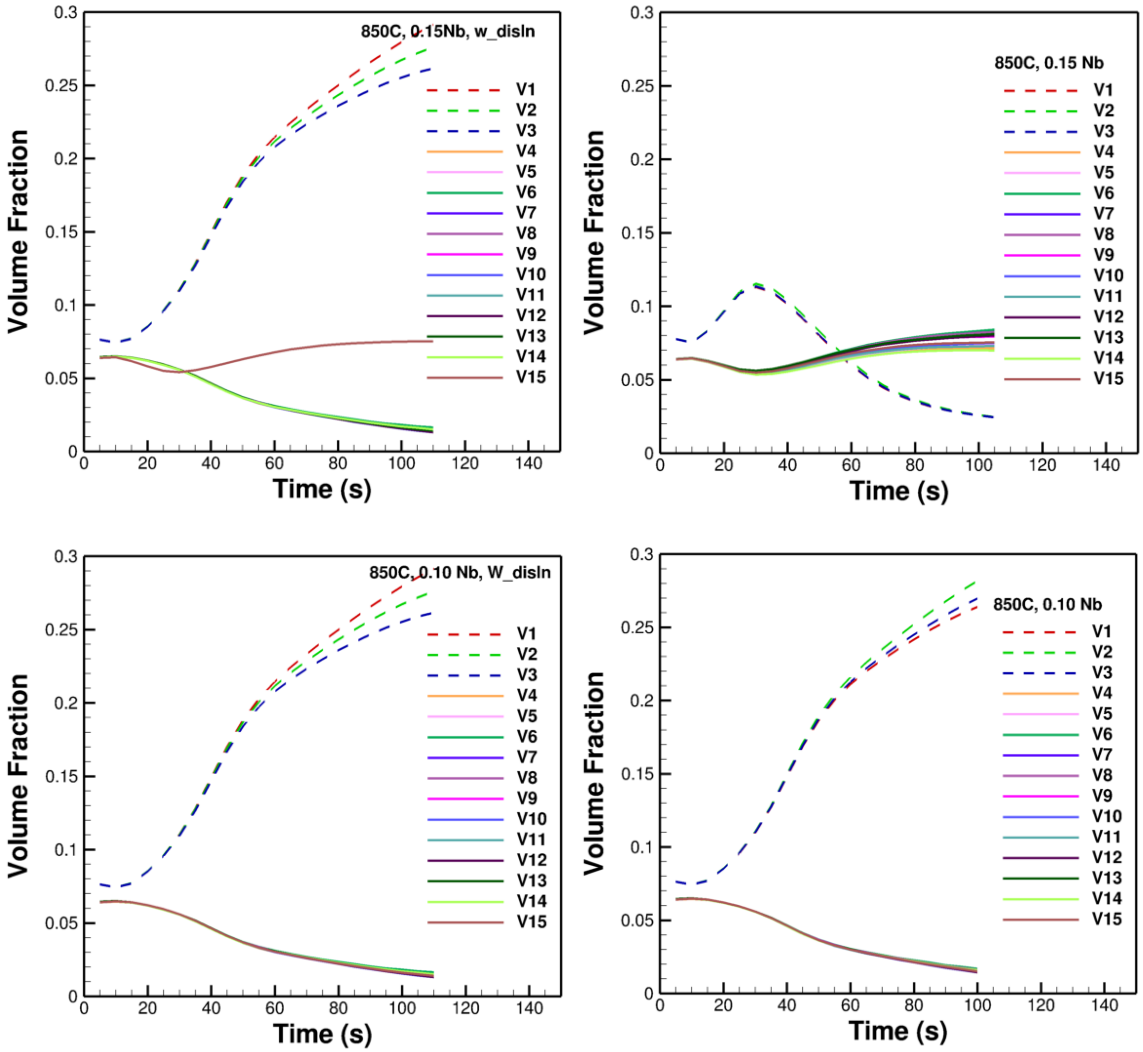

Figure 24. Relative nucleation and growth of γ" and δ variants at 850°C as a function of alloy composition and dislocation strain field.

A significant change in the stability of the δ phase relative to that of γ" occurs at an annealing temperature of 850°C is shown in Figure 24, especially for the lower Nb alloys (0.10 and 015 Nb). While for the 0.20Nb alloy, the δ phase ultimately overtakes the growth of the γ" phase that nucleates at early times, for the 0.10Nb alloy, the γ" phase ends up as the dominant phase fully consuming the δ. This seems to indicate that for the 0.10 Nb alloy at 850°C, the increased driving force for the δ phase is not sufficient to form supercritical nuclei of the δ phase that can grow and consume the γ" phase. Therefore, the volume fraction of the δ phase appears to be nucleation controlled. For the 0.15Nb alloy, the temporal evolution at 850°C seems to show some interesting trends. This case shows a clear example of how the γ" phase nucleation and growth can be promoted over the δ phase due to the presence of the dislocation strain field. It can be seen that in the absence of the dislocation, δ is the dominant phase, while γ" is dominant in the presence of the dislocation strain field. It is also interesting to note that one of the δ variants, variant 15 seems to be promoted at the expense of others, in the presence of the dislocation strain field.

In the parametric simulations above in Figures 21-24, the concentration of the entire simulation volume was set equal to the local alloy concentration at specific locations in the interdendritic region of the solidification structure. However, there is a steep concentration gradient due to micro segregation whose length scale is set by the primary / secondary arm spacing in the solidification microstructure. Such concentration gradients are also possible in a partially homogenized alloys as described earlier due to the dissolution of the Laves phase. Simulations were carried out in a simulation volume which is 126 nm along each edge, with the concentration in the middle of the domain set to 0.25Nb while at the edge it is set to 0.08Nb. The Fe concentration is set to be uniform at 0.379Nb. The simulations were carried out with or without the presence of a dislocation line. The results are summarized in Figure 25. Very significant differences are noticed between the phase selection results shown in Figures 21-24 versus Figure 25. In the presence of the lateral Nb concentration gradient, the peak γ" volume fraction prior to its reduction at the expense of growing δ phase is appreciably higher than in the uniform concentration case. Second, there is a significant spread in the volume fractions of the different δ variants in the domain with a Nb-concentration gradient compared to the domains uniform Nb concentration. Third, the stabilization of the γ" phase against the δ phase seen in the uniformly low Nb domain at 850°C is absent in the presence of the initial Nb concentration gradient. It appears that a specific variant (variant 6) of the δ phase grows preferentially compared to all other variants at 850°C in the presence of the Nb concentration gradient. The concentration gradient, and initial high and low Nb concentrations have to be controlled such that a gradient γ" precipitation can be promoted through direct aging without precipitating the δ phase. Further parametric studies with varying gradient concentrations have to be performed to identify the optimum conditions under which this objective can be achieved.

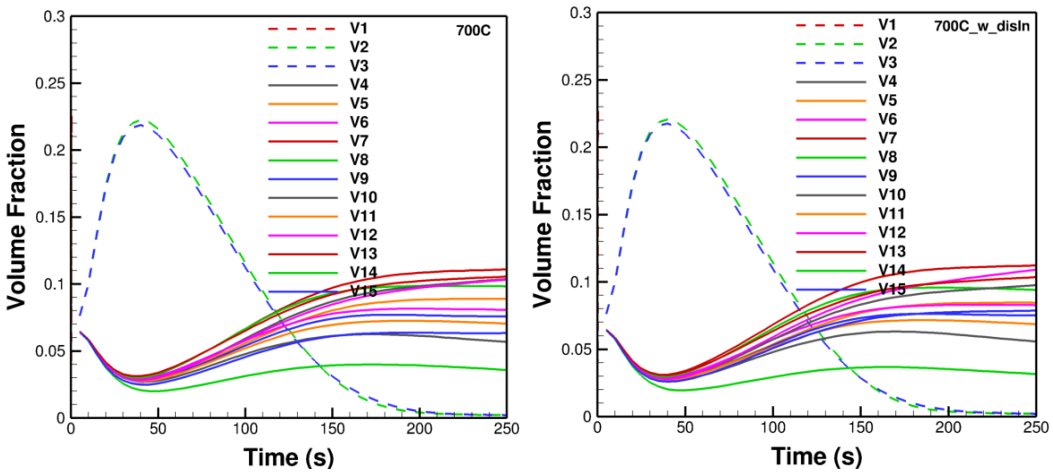

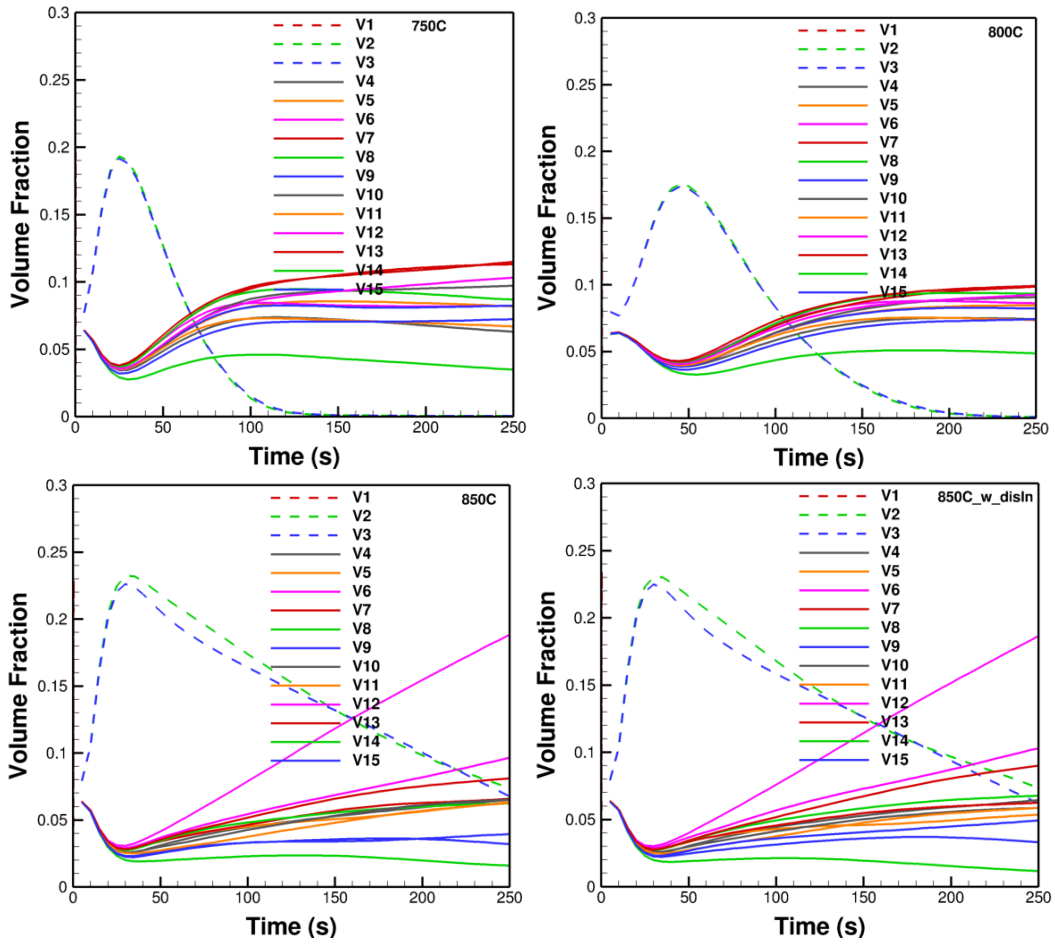

Figure 25. Parametric studies with a lateral Nb concentration gradient in the simulation domain

3. SUMMARY

MEUMAPPS-SS phase field simulations using HPC capabilities were used to understand the nucleation and growth of crystallographic variants of γ", γ', and δ phase during direct aging of Ni-Fe-Nb alloy which is the surrogate ternary alloy for IN718 used in the simulations. Direct aging offers an attractive alternative to complete homogenization of the solidification microstructure followed by aging because (1) it offers significant energy savings, and (2) it maintains the fine grain size obtained as a result of the rapid solidification under AM conditions. Opportunities exist for tailoring the solute concentration gradients in the as-built microstructure through partial homogenization that results in the dissolution of the detrimental Laves phase and a reduction in the spatial length scale of the solute gradients. The simulations focused on identifying conditions under which the γ" phase can preferentially nucleate and grow during aging of partially homogenized microstructures. Parametric studies using various Nb concentrations and annealing temperatures with or without the dislocation strain field indicated that γ" can be made to nucleate and grow and remain stable against the δ phase when annealing is carried out at 850°C in microstructures where the maximum Nb content is reduced to below 0.15. However, when these simulations were carried out in domains containing a Nb concentration gradient, the stability of γ" was reduced and a specific variant of δ phase seemed to grow preferentially with or without the dislocation strain field. Additional

simulations using larger domains and /or shallower concentration gradients than the ones used in these simulations have to be performed in order to optimize the microstructures in which the stability of the γ" phase can be made more robust. In addition, the simulations must be extended to more complex dislocation configurations than the straight edge dislocation considered in the present simulations, as well as to domains containing multiple dendrite orientations.

The MEUMAPPS-SS phase field code is constantly undergoing upgrades both in the accuracy of the thermodynamic linkage with specific alloy systems as well as in the nucleation models. As mentioned earlier, the Gibbs free energy functions for the phases are approximated as second-degree polynomials as a function of the concentration of the solutes. The main advantage of this formulation is that the derivatives of the free energy with respect to composition become linear functions of the solute concentrations. This is very convenient because the calculation of the concentrations at the diffuse interfaces is reduced to solving a system of linear equations in solute concentrations. However, the free-energy functions of precipitates with a very narrow range of solute solubility in them tend to be very deep concave surfaces and require higher order polynomials to better fit the surfaces near the minimum cusps. However, the use of higher order polynomials would require an iterative solve for the interface concentrations that is time-consuming and adds to already time-consuming iterative solve used for converging the displacements in the elasticity problem associated with eigenstrains. Another limitation in the simulations is the use of Langevin noise for the nucleation of phases. While this approach is very convenient when only a single precipitating phase is involved, and the undercooling is high, it becomes very difficult to implement the model when multiple phases with different nucleation barriers are involved. There is additional complexity due to the presence of composition gradient in the matrix because the nucleation kinetics is closely connected with the local alloy composition, and therefore optimizing the noise parameters to precipitate multiple phases in the presence of composition gradients becomes very challenging. Current improvements to the code that focused on (1) evaluating higher order polynomial representations of free energies with an iterative solver and (2) implementing a thermodynamically consistent nucleation model proposed by Thompson and Spaepen [12], that eliminates the need for introducing Langevin noise.

4. REFERENCES

1. S.G. Kim, W.T. Kim, and T. Suzuki, “Phase-field model for binary alloys,” Phys. Rev. E., 60, 7186-7197 (1999).
2. N. Zhou et al., “Computer simulation of phase transformation and plastic deformation in IN718 superalloy: Microstructural evolution during precipitation,” Acta Mater. 65, 270-286 (2014)
3. I. Steinbach and M. Apel, “Multi phase field model for the solid-state transformation with elastic strain, Physica D, 217, 153-160 (2006).
4. L.Q. Chen and J. Shen, “Applications of semi-implicit Fourier-spectral method to phase field equations,” Comp. Phys. Comm. 108, 147-158 (1998).
5. D. Pekurovsky, “P3DFFT: A framework for parallel computations of Fourier transforms in three dimensions,” SIAM Journal of Scientific Computing, 4, C192-C209 (2012).
6. J. A. Turner et al., “ExaAM: Metal additive manufacturing simulation at the fidelity of the microstructure,” International Journal of High-Performance Computing Applications, 36, 13-39, 2022.
7. B. Radhakrishnan, G. B. Sarma, Y. Song, and J. A. Turner, “Phase filed simulations of co-precipitation in AM processed 625 and 718 alloys during post-process anneal,” 15th U.S. National Congress on Computational Mechanics (USNCCM-15), Austin, Texas, July 30, 2019.

8. Y. Song, B. Radhakrishnan, R. Acharya, “Simulating the evolution of γ'/γ" precipitates in the inter-dendritic regions of additively manufactured IN718 due to post-processing heat treatments, TMS, 2020.
9. Y. Song, B. Radhakrishnan, S. Gorti, and R. Acharya, “Precipitate Growth Kinetics under Inhomogeneous Concentration Fields using a Phase-field Model,” Physical Review Materials, 5, 053401 (2021).
10. T. G. Gallmeyer et al., “Knowledge of process-structure-property relationships to engineer better heat treatments for laser powder bed fusion additive manufactured Inconel,” Additive Manufacturing, 31, 100977 (2020).
11. H. Liu, B. Bellón, and J. LLorca, “Multiscale modelling of the morphology and spatial distribution of θ' precipitates in Al-Cu alloys,” Acta Materialia, 132, 611-626 (2017).
12. C. V. Thompson and F. Spaepen, “Homogeneous crystal nucleation in binary metallic melts,” Acta metal. 31, 2021-2027 (1983).

ACKNOWLEDGMENTS

This research was supported by the High-Performance Computing for Manufacturing (HPC4Mfg) program sponsored by the Advanced Manufacturing Office of the U.S. Department of Energy (DOE), and by the Exascale Computing Project (17-SC-20-SC), a collaborative effort of the U.S. DOE Office of Science and the National Nuclear Security Administration. This research used resources of the Oak Ridge Leadership Computing Facility, which is a DOE Office of Science User Facility supported under contract DE- AC05-00OR22725. Research performed at the Oak Ridge National Laboratory (ORNL), managed by UT-Battelle, LLC, under Contract No. DE-AC05-00OR22725 for the U.S. DOE.